ANNUAL REVIEWS

Atmospheric CO_2 over the Past 66 Million Years from Marine Archives

James W.B. Rae,[1] Yi Ge Zhang,[2] Xiaoqing Liu,[2] Gavin L. Foster,[3] Heather M. Stoll,[4] and Ross D.M. Whiteford[1]

[1] School of Earth and Environmental Sciences, University of St Andrews, St Andrews KY16 9AL, United Kingdom; email: jwbr@st-andrews.ac.uk

[2] Department of Oceanography, Texas A&M University, College Station, Texas 77843, USA

[3] School of Ocean and Earth Science, National Oceanography Centre Southampton, University of Southampton, Southampton SO14 3ZH, United Kingdom

[4] Department of Earth Sciences, ETH Zürich, 8092 Zürich, Switzerland

ANNUAL REVIEWS CONNECT

www.annualreviews.org

- Download figures
- Navigate cited references
- Keyword search
- Explore related articles
- Share via email or social media

Keywords

CO_2, boron isotopes, alkenones, climate, Cenozoic

Abstract

Throughout Earth's history, CO_2 is thought to have exerted a fundamental control on environmental change. Here we review and revise CO_2 reconstructions from boron isotopes in carbonates and carbon isotopes in organic matter over the Cenozoic—the past 66 million years. We find close coupling between CO_2 and climate throughout the Cenozoic, with peak CO_2 levels of ~1,500 ppm in the Eocene greenhouse, decreasing to ~500 ppm in the Miocene, and falling further into the ice age world of the Plio–Pleistocene. Around two-thirds of Cenozoic CO_2 drawdown is explained by an increase in the ratio of ocean alkalinity to dissolved inorganic carbon, likely linked to a change in the balance of weathering to outgassing, with the remaining one-third due to changing ocean temperature and major ion composition. Earth system climate sensitivity is explored and may vary between different time intervals. The Cenozoic CO_2 record highlights the truly geological scale of anthropogenic CO_2 change: Current CO_2 levels were last seen around 3 million years ago, and major cuts in emissions are required to prevent a return to the CO_2 levels of the Miocene or Eocene in the coming century.

- CO_2 reconstructions over the past 66 Myr from boron isotopes and alkenones are reviewed and re-evaluated.

- CO_2 estimates from the different proxies show close agreement, yielding a consistent picture of the evolution of the ocean-atmosphere CO_2 system over the Cenozoic.
- CO_2 and climate are coupled throughout the past 66 Myr, providing broad constraints on Earth system climate sensitivity.
- Twenty-first-century carbon emissions have the potential to return CO_2 to levels not seen since the much warmer climates of Earth's distant past.

1. RECONSTRUCTING ANCIENT CO$_2$: WHY AND HOW?

An atmosphere of that [CO_2] gas would give to our earth a high temperature; and if as some suppose, at one period of its history the air had mixed with it a larger proportion than at present, an increased temperature . . . must have necessarily resulted.

—Eunice Newton Foote (1856, p. 383), the first scientist to demonstrate the heat-trapping properties of CO_2, goes on to describe the potential for CO_2-driven climate change in the geological record, in her pioneering paper in 1856

Through its effect on Earth's radiation budget, atmospheric CO_2 is a major contributor to climate change, both past and present (Arrhenius 1896, Lacis et al. 2010, Rohling et al. 2012). As a weak acid, CO_2 is also intimately linked to the chemistry of the ocean and is capable of driving rapid ocean acidification (Caldeira & Wickett 2003, Hönisch et al. 2012). Understanding the behavior of CO_2 within the Earth system—including the interactions and feedbacks that govern the global carbon cycle—is thus a scientific goal with major societal significance (Gattuso et al. 2015b, Masson-Delmotte et al. 2018).

The geological record contains abundant examples of major changes in the carbon cycle (Hönisch et al. 2012). Rapid carbon injection from volcanoes and/or organic carbon reservoirs has repeatedly driven episodes of ocean acidification and global warming (Gutjahr et al. 2017, Müller et al. 2020, Penman et al. 2014), often associated with mass extinctions (Jurikova et al. 2020). And while rapid CO_2 change has repeatedly posed a challenge to life on Earth, the long-term regulation of CO_2 has ultimately maintained our planet's habitability (Kasting 2019). The patterns and processes of paleo-CO_2 change not only are fascinating in their own right but also, importantly, can inform our understanding of the impact of future CO_2 change (Rohling et al. 2012, Royer 2016).

Yet despite the importance of CO_2 in our planet's past and future, reconstructions of CO_2 change through geological time have, until recently, been relatively sparse and, in some intervals, hard to interpret. For instance, while the pioneering CO_2 reconstructions of Pearson & Palmer (1999, 2000) and Pagani et al. (1999, 2005) show a decrease in mean values as climate cools over the past 50 million years (see Zachos et al. 2008, figure 2), the high amplitude variability in the earlier portions of these records and the relative stability in their later parts are hard to explain. In recent years, substantial progress has been made in methods of CO_2 reconstruction and their application to the geological record (Anagnostou et al. 2016, Beerling & Royer 2011, Bolton & Stoll 2013, Dyez et al. 2018, Foster & Rae 2016, Jurikova et al. 2020, Witkowski et al. 2018, Zhang et al. 2013) (see **Supplemental Table 1**). Here we review CO_2 reconstructions from two widely used and rapidly growing methods: carbon isotopes in alkenones and boron isotopes in planktic foraminifera. These methods have been the focus of much of the recent work by our research groups, and we hope that the re-evaluation provided here will provide a useful contribution to wider efforts to combine a broader range of paleo-CO_2 proxies (see **Supplemental Table 1**; and

Alkenones:
long-chain (C_{36}–C_{39}) di-, tri-, and tetra-unsaturated ethyl and methyl ketones; alkenones in sediments are commonly used as biomarkers of haptophyte algae

Foraminifera:
single-celled amoeba-like organisms; many produce calcite shells, which are common in marine cores and widely used in environmental reconstruction

Supplemental Material >
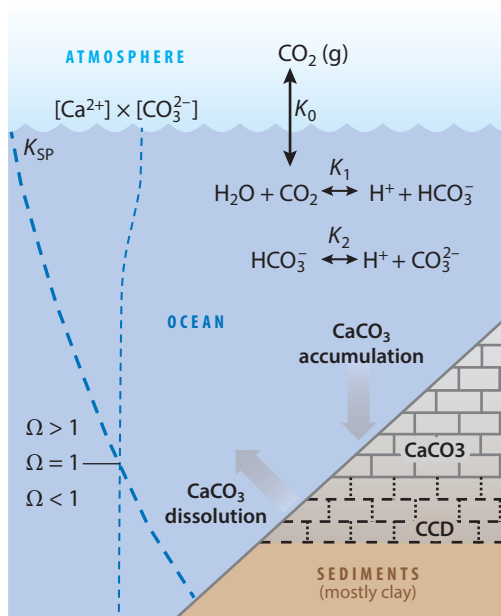
Figure 1

The CO_2 system of the atmosphere, the ocean, and its sediments. The equilibrium between CO_2 gas in the atmosphere and dissolved aqueous CO_2 in seawater is set by K_0, the Henry's law constant. Dissolved CO_2 then reacts with water to form HCO_3^- and CO_3^{2-}, with K_1 and K_2 denoting the equilibrium constants of these reactions. Much of the seafloor is coated by calcium carbonate ($CaCO_3$) sediments, including coral reefs in shallow waters and the fallen shells of planktonic carbonate producers in the deep sea. $CaCO_3$ accumulates provided that the product of its ingredients ($[Ca^{2+}] \times [CO_3^{2-}]$) is greater than K_{SP} (the solubility product); this ratio sets the saturation state of seawater, denoted Ω (i.e., $\Omega = [Ca^{2+}] \times [CO_3^{2-}]/K_{SP}$). K_{SP} is strongly pressure dependent, so Ω of calcite (the predominant form of oceanic $CaCO_3$) decreases from ~6 in warm surface waters to less than 1 in the abyss. This causes a sharp increase in $CaCO_3$ dissolution at depth: The carbonate compensation depth (CCD) is the level where carbonate dissolution balances the rain of pelagic carbonate. Below this depth, little $CaCO_3$ is found in sediments, which are dominated by clay.

see **https://www.paleo-co2.org**). We focus on the Cenozoic—the past 66 million years—where marine-based CO_2 reconstructions can be readily compared to abundant marine-based reconstructions of climate (Evans et al. 2018, Herbert et al. 2016, Lear et al. 2000, Tierney et al. 2019a, Zachos et al. 2001). During this era, climate evolves from the warm greenhouse world of the Eocene to the ice-clad world of the recent ice ages, motivating study of the role of CO_2 in this major transition (Westerhold et al. 2020, Zachos et al. 2001).

In this review, we provide a brief overview of CO_2's behavior in seawater (Section 2) before reviewing and updating CO_2 records from alkenones (Section 3) and boron isotopes (Section 4), building a consistent picture of the Cenozoic CO_2 system (Section 5). We discuss potential controls on long-term CO_2 change (Section 6) and the long-term coupling of CO_2 and climate apparent in these data (Section 7), and we then place current and future CO_2 change in the context of the geological record (Section 8).

2. CO_2 IN SEAWATER

CO_2 is an unusual gas, in that its main reservoir at Earth's surface is not the atmosphere but the ocean (see **Figure 1** and the sidebar titled CO_2: Concentration Versus Partial Pressure). This

CO$_2$: Concentration Versus Partial Pressure

Atmospheric CO$_2$ is commonly expressed as a partial pressure (pCO$_2$, in units of microatmospheres) or as a concentration or mole fraction (CO$_2$ or xCO$_2$, in units of parts per million), which are related by this formula:

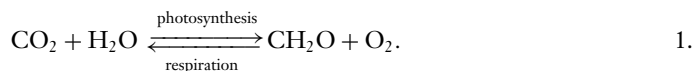$$p\text{CO}_2 \ (\mu\text{atm}) = (p_{\text{total}} - p\text{H}_2\text{O}) \ \times \ x\text{CO}_2 \ (\text{ppm}).$$

In dry air (pH$_2$O $= 0$) with a total pressure of 1 atm ($p_{\text{total}} = 1$), partial pressure and mole fraction are equal. However air equilibrated with seawater is typically assumed to have 100% humidity. As a result, pCO$_2$ is lower than xCO$_2$, by $\sim$3% at 25°C and $\sim$6% at 35°C. For warm conditions with high CO$_2$ levels, pCO$_2$ may therefore be around 100 ppm lower than CO$_2$ concentration. It is thus important that these terms are not used interchangeably. We note that pCO$_2$ is the physical property that drives ocean-atmosphere CO$_2$ exchange (**Figure 2**), while CO$_2$ concentrations are typically reported for ice core data and used as input for climate models and in future climate change scenarios. Unless otherwise specified, in this review we report atmospheric CO$_2$ concentration (or mole fraction) in units of parts per million by volume (equivalent to μmol/mol).

results from the reaction between CO$_2$[1] and water to form bicarbonate (HCO$_3^-$) and carbonate ion (CO$_3^{2-}$). These dissolved inorganic carbon (DIC) species are linked by a series of acid-base reactions (**Figure 1**).
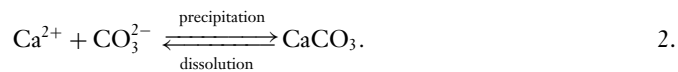
As CO$_2$ is readily exchanged between the ocean and the atmosphere (**Figure 2**), the state of the ocean's CO$_2$ chemistry is largely responsible for setting atmospheric CO$_2$. If ocean pH is low, the reactions in **Figure 1** get pushed toward the CO$_2$ end (right to left), elevating dissolved [CO$_2$] in surface waters and CO$_2$ gas in the atmosphere; if ocean pH is high, the reactions go from left to right, elevating [CO$_3^{2-}$] and lowering CO$_2$.

Ocean pH, in turn, is set by the balance between alkalinity (which tracks the strong acids and bases in seawater) (see the sidebar titled Alkalinity) and DIC (seawater's most abundant weak acid-base system). If the major ion chemistry of the ocean gives high alkalinity (i.e., a large excess of strong base cations such as Na$^+$ and Ca^{2+} relative to strong acid anions such as Cl$^-$ and SO$_4^{2-}$), and if the pool of DIC is relatively small, the carbonate system must be pulled toward doubly charged CO$_3^{2-}$ to maintain charge balance. Conversely, if a large pool of DIC exists but alkalinity is small, much of the DIC must be present as uncharged CO$_2$. The control of alkalinity and DIC on seawater CO$_2$ chemistry is illustrated by the contour plot in **Figure 3**. Note that knowledge of any two carbonate system parameters (CO$_2$, HCO$_3^-$, CO$_3^{2-}$, alkalinity, DIC, pH) allows the rest of the carbonate system to be determined.

Changes in alkalinity and DIC come about through biogeochemical reactions. Within the ocean, photosynthesis draws down DIC to make organic matter, which may be remineralized back to DIC by respiration:

$$\text{CO}_2 + \text{H}_2\text{O} \underset{\text{respiration}}{\overset{\text{photosynthesis}}{\rightleftharpoons}} \text{CH}_2\text{O} + \text{O}_2. \qquad 1.$$

Dissolved inorganic carbon (DIC): the sum of dissolved CO$_2$, bicarbonate (HCO$_3^-$), and carbonate ion (CO$_3^{2-}$)—i.e., DIC = [CO$_2$] + [HCO$_3^-$] + [CO$_3^{2-}$]

The cycling of CaCO$_3$ is also important, with precipitation of CaCO$_3$ (typically by biocalcification in the modern ocean) consuming two equivalents of alkalinity per mole of DIC. CaCO$_3$ dissolution on the seafloor rereleases alkalinity and DIC in a 2:1 ratio:

$$\text{Ca}^{2+} + \text{CO}_3^{2-} \underset{\text{dissolution}}{\overset{\text{precipitation}}{\rightleftharpoons}} \text{CaCO}_3. \qquad 2.$$

---

[1]We use dissolved CO$_2$ concentration [CO$_2$] to refer to aqueous CO$_2$ [CO$_2$ (aq)] plus carbonic acid [H$_2$CO$_3$]; CO$_2$ (aq) is $\sim$300 times more abundant than H$_2$CO$_3$.

Ocean-atmosphere pCO$_2$ (μatm)
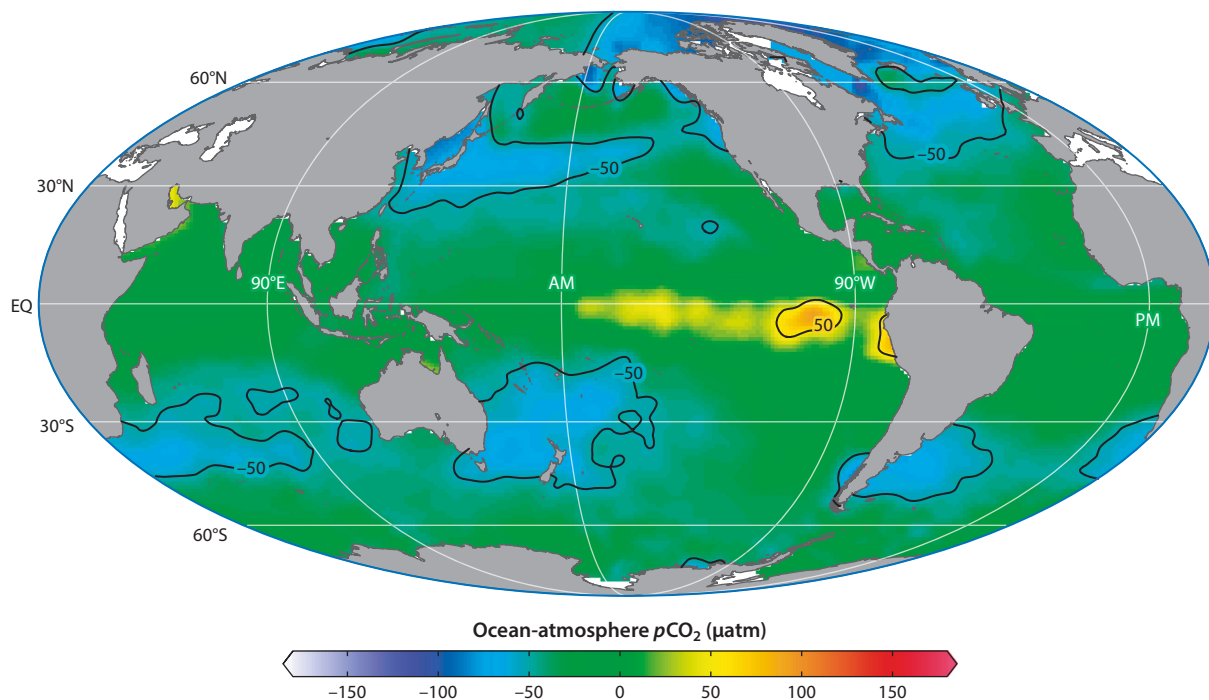
Figure 2

Difference in partial pressure of CO$_2$ between the surface ocean and the atmosphere. Atmospheric reconstructions can be obtained from the marine realm because CO$_2$ cycles rapidly between the surface ocean and the atmosphere, with large tracts of the ocean's surface—in particular in the subtropics—maintaining close equilibrium with the atmosphere (contours indicating $\pm$50 μatm). Surface water pCO$_2$ is higher than the atmosphere (*red colors*) in some upwelling regions (e.g., the Eastern Equatorial Pacific) where CO$_2$-rich waters are brought to the surface, although this is partially offset by cooler temperatures (see **Supplemental Figure 1**). Surface water pCO$_2$ values lower than the atmosphere (*blue colors*) are found at mid-latitudes where surface waters from the subtropics, previously in equilibrium with the atmosphere, are cooled. The annual average gridded climatology data are from Takahashi et al. (2014), referenced to 2005 (with atmospheric CO$_2$ of 400 μatm), plotted using Ocean Data View.

Supplemental Material >

ALKALINITY

Alkalinity is a central concept in CO$_2$ chemistry and, unfortunately, a common source of confusion.

Alkalinity is measured by titration of seawater with strong acid. The H$^+$ from the acid combines with the CO$_3^{2-}$ and HCO$_3^-$ in seawater to form CO$_2$. The greater the concentration of CO$_3^{2-}$ and HCO$_3^-$, the greater the addition of H$^+$ to reach the titration's CO$_2$ endpoint, and the higher the alkalinity. But what sets the abundance of CO$_3^{2-}$ and HCO$_3^-$ in the first place? This is best answered by considering that all solutions maintain charge balance. Summing the charges of the major elements (or strictly speaking, the strong bases and acids, which are fully dissociated and do not change their speciation as a function of pH) in seawater (Na$^+$ + K$^+$ + 2 $\times$ Mg^{2+} + 2 $\times$ Ca^{2+} ... versus Cl$^-$ + 2 $\times$ SO$_4^{2-}$ + ...) reveals an excess of positive charge. Charge balance is maintained by the sum of negative charges from HCO$_3^-$ and 2 $\times$ CO$_3^{2-}$ (plus other minor weak acid base species). We thus arrive back at our original analytical definition of alkalinity via consideration of major element charge imbalance, which provides an alternative definition and may be usefully linked to biogeochemical reactions. (For more detail, see Zeebe & Wolf-Gladrow 2001 and Middelburg et al. 2020.)
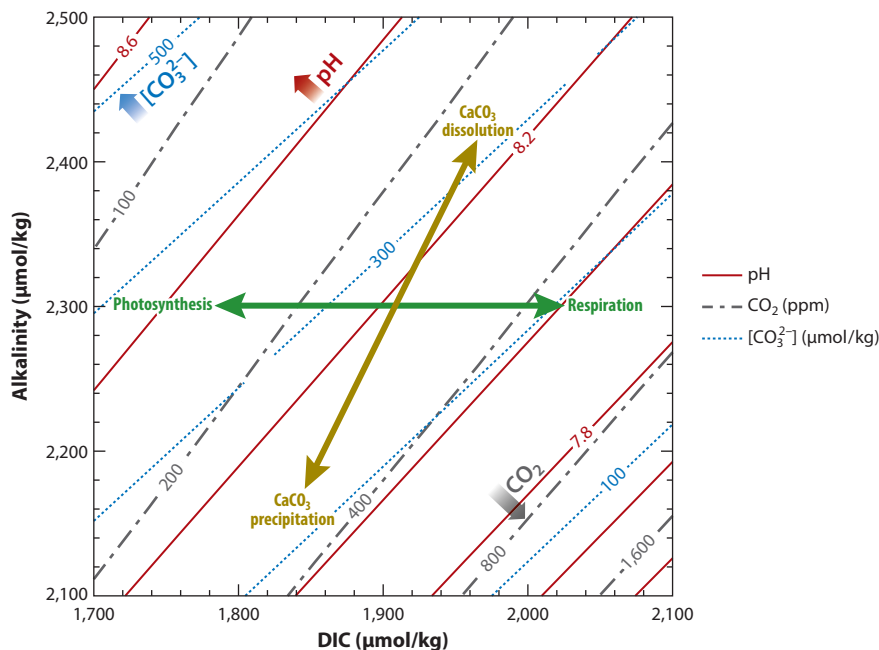
Figure 3

Relationships between key components of the CO_2 system as a function of the master variables, alkalinity and dissolved inorganic carbon (DIC). CO_2 contours show the atmospheric CO_2 concentration (in parts per million by volume) in equilibrium with this water. pH, CO_2, and $[CO_3^{2-}]$ have roughly parallel contours in alkalinity-DIC space with a slope of ∼1. When alkalinity is high relative to DIC, pH and $[CO_3^{2-}]$ are high and CO_2 is low; when DIC is high relative to alkalinity, pH and $[CO_3^{2-}]$ are low and CO_2 is high. Note that the equilibrium constants of the carbonate system (**Figure 1**) are influenced by temperature, pressure, salinity, and the major ion composition of seawater (due to ion pairing interactions). This plot is shown for 25°C, 35 psu, sea surface pressure, and $[Ca^{2+}]$, $[Mg^{2+}]$, and $[SO_4^{2-}]$ at their modern values; changes to these values will slightly alter the slopes of these contours. In contrast, alkalinity and DIC are conservative and do not change as a function of temperature or pressure, and they scale linearly with changes in salinity.

On longer timescales, alkalinity is supplied to the ocean by chemical weathering reactions, which release strong base cations from silicate rocks. The following reaction between a silicate mineral (wollastonite) and CO_2 dissolved in water represents an addition of two equivalents of alkalinity with no net change in DIC:

$$CaSiO_3 + 2CO_2 + H_2O \rightarrow Ca^{2+} + 2HCO_3^- + H_4SiO_4^0. \qquad 3.$$

Coupling alkalinity supply through weathering (Equation 3) and removal by carbonate precipitation (Equation 2) gives the simplified Urey reaction (Urey 1952), which is commonly used to conceptualize silicate weathering's influence on CO_2:

$$CaSiO_3 + CO_2 \underset{\text{metamorphism}}{\overset{\text{weathering}}{\rightleftharpoons}} CaCO_3 + SiO_2. \qquad 4.$$
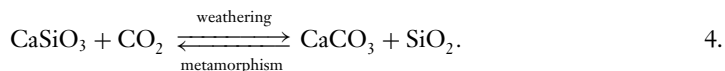
The reverse of this reaction represents thermal decarbonation during metamorphism of carbonate rocks.

These CO_2 system concepts are central in reconstructing atmospheric CO_2 from marine archives, via either determination of dissolved CO_2 using alkenone $\delta^{13}C$ (Section 3) or determination of pH from foraminiferal $\delta^{11}B$ (Section 4). They are also important for consideration of

the mechanisms of CO_2 change due to their roles in setting the alkalinity and DIC of the ocean-atmosphere CO_2 system (Section 6). (For more detailed treatment of seawater's CO_2 chemistry, see Zeebe & Wolf-Gladrow 2001 and Sarmiento & Gruber 2006.)

3. ALKENONE-BASED CO_2 RECONSTRUCTIONS

The phytoplankton CO_2 proxy is based on a relationship between dissolved CO_2 concentration and the photosynthetic fractionation of carbon isotopes in organic matter (ε_p) that has been fixed by marine photosynthetic algae (Freeman & Hayes 1992) (see the schematic in **Supplemental Figure 2**). While early research used bulk organic matter and kerogen to determine ε_p (Dean et al. 1986), advances in analytics have allowed the majority of recent isotopic analyses to be made on specific molecular compounds (Hayes et al. 1990). These include geoporphyrins (Popp et al. 1989), pristane, and phytane (Freeman & Hayes 1992, Naafs et al. 2016, Witkowski et al. 2018), all of which are chlorophyll diagenetic products, as well as a group of long-chain ketones called alkenones, which are produced by a few species of haptophyte algae in the modern ocean and which are more abundant in the Neogene but also found in Paleogene and Cretaceous sediments (Brassell 2014). Biomineral-bound organic carbon has also been used to measure photosynthetic carbon isotope fractionation of fossil diatoms, and diatom-specific sterols have been measured in water column samples (Heureux & Rickaby 2015, Mejía et al. 2017, Pancost et al. 1997). Analysis of carbon isotopes in individually picked organic-walled dinoflagellates is also under development (Sluijs et al. 2018).

In this review, we focus on the application of the phytoplankton proxy using alkenones, as they have been the most widely applied phase for ε_p determination. It is clear that alkenone ε_p is sensitive to changes in CO_2, but significant evolution in understanding of the proxy in the past decade (Badger et al. 2019; Stoll et al. 2019; Zhang et al. 2019, 2020) has led to new procedures for estimating CO_2 from a given ε_p for many time periods in the past. As a consequence, the most accurate interpretation of the proxy lies in updated recalculation of CO_2 rather than compilation of as-published CO_2 estimates. We review these advances and the important gaps that affect confidence in CO_2 estimations, and we acknowledge that future revisions to absolute CO_2 calculations will be important as the calibration database becomes more robust and our understanding of the physiology of the extinct phytoplankton species improves.

### 3.1. The Evolution of Alkenone-Based CO_2 Reconstructions

A large number of ε_p determinations from alkenones have been made on timescales spanning the Eocene through the Pleistocene. Notably, in their raw form these ε_p records show similar structure to the Cenozoic benthic $\delta^{18}O$ record (**Figure 4**), suggestive of long-term coupling between CO_2 and global climate, although offsets in absolute ε_p values are apparent between core sites. To estimate CO_2, most of these studies have assumed a hyperbolic increase in ε_p with $1/CO_2$ based on application of a theoretical model of carbon uptake by phytoplankton cells (Laws et al. 1995, Popp et al. 1998, Rau et al. 1996). This interpretative framework for phytoplankton ε_p is based on the principle of diffusive CO_2 uptake into a single compartment cell driven by the gradient established by the rate of carbon fixation. This model also illustrates how higher phytoplankton growth rate and larger cell radius would be expected to lower ε_p, and higher cellular permeability could increase ε_p (Rau et al. 1996, Popp et al. 1989).

Most commonly, an empirical hyperbolic solution has been established whereby the dissolved seawater $[CO_2]$ is equated to ε_p through the use of a coefficient *b*, which should encompass a series of physiological, non-CO_2 influences on fractionation, and by referencing to ε_f, the assumed 25‰ maximum enzymatic fractionation by Rubisco, the enzyme responsible for photosynthetic

ε_p: the carbon isotope fractionation between aqueous CO_2 and phytoplankton biomass, the $\delta^{13}C$ of which can be estimated from foraminifera and alkenones, respectively

Haptophytes: a clade of photosynthetic algae, including the calcareous plate-bearing coccolithophores (some of the most abundant open ocean phytoplankton), and species that lack coccolith plates
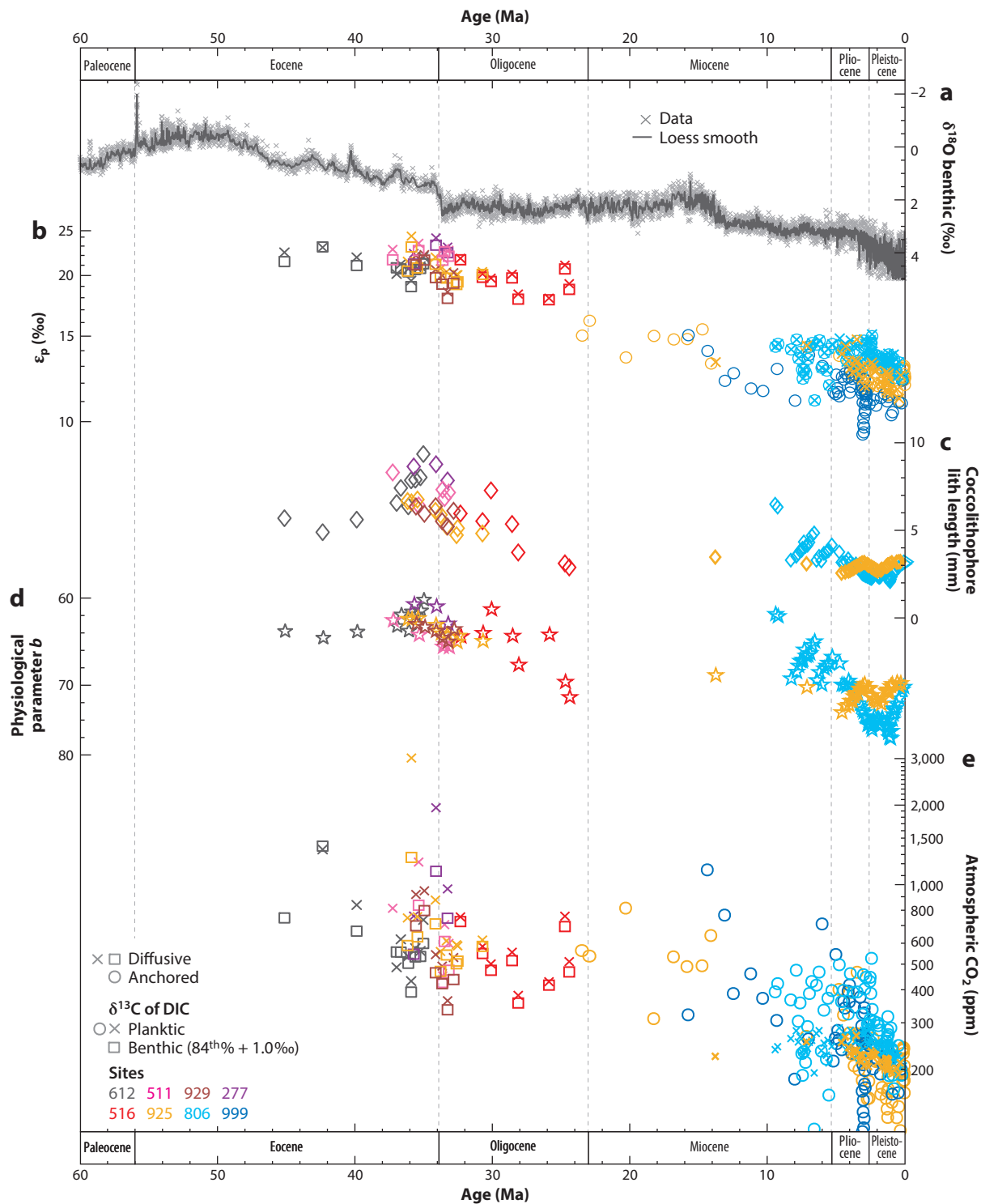
(*Caption appears on following page*)

Figure 4 (*Figure appears on preceding page*)

Updated CO_2 reconstructions from alkenone $\delta^{13}C$. (*a*) Benthic $\delta^{18}O$ from Westerhold et al. (2020); individual data points in gray crosses with loess smooth in dark gray line. (*b*) Carbon isotope fractionation (ε_p) between the phytoplankton biomass and aqueous CO_2. $\delta^{13}C$ of dissolved inorganic carbon (DIC) estimates are shown from planktic foraminifera (corrected for vital effects) (*crosses* and *circles*) and also, in the older part of the record, from the upper range (eighty-fourth percentile) of the benthic $\delta^{13}C$ stack plus an offset of 1.0‰ (*squares*) to give a representative surface ocean value less influenced by planktic $\delta^{13}C$ vital effects, which are less well constrained in this interval. (*c*) Measured coccolithophore lith length. (*d*) *b* values used in updated ε_p to CO_2 calculation following Zhang et al. (2020) that use measured coccolith lengths to inform coupled changes in cell size and growth rate. (*e*) CO_2 calculated following Zhang et al. (2020) (*open squares* and *crosses*) and also, for the Neogene, by late Quaternary anchoring (*open circles*), informed by the culture study of Stoll et al. (2019). Note that a couple of anomalous high CO_2 points around 35 Ma are the result of anomalous planktic $\delta^{13}C$; the approach using an offset from the benthic stack gives more coherent values. Different sites are indicated by symbol color, as described in the legend. Data are from Badger et al. (2019), Bolton & Hernández-Sánchez (2016), Pagani et al. (2005, 2010, 2011), and Zhang et al. (2013, 2017), with calculations as described in the text. All data are available as online **Supplemental Material**.

carbon fixation:

$$\varepsilon_p = \varepsilon_f - \frac{b}{[CO_2]}. \qquad\qquad 5.$$

This relationship has been used for establishing nearly all alkenone-based CO_2 records to date, using an estimation of the appropriate value of *b* to be applied in ancient settings. Most commonly, the *b* value has been deduced for modern oceanographic settings and has been assumed to remain constant for that location in the past. Typically, the *b* value for the modern setting has been inferred from analysis of ε_p in modern water column phytoplankton or by applying a regression between *b* and the concentration of a major nutrient, $[PO_4]$, derived from spatial variations in ε_p in phytoplankton throughout the modern surface ocean (Bidigare et al. 1997).

Several lines of evidence now suggest that this calibration approach requires revision to yield accurate estimates of absolute past CO_2. Study of ε_p over Pleistocene glacial-interglacial cycles for which CO_2 is independently constrained by ice core records (Bereiter et al. 2015) shows that, in every site explored, these inferred non-CO_2 effects (*b*) are highest during the interglacial and lowest during the glacial (Badger et al. 2019, Stoll et al. 2019, Zhang et al. 2019). At the same time, the present-day (photic zone) correlations between the physiological parameter (*b*) and $[PO_4]$ are not broadly representative of the past (Zhang et al. 2019). Analogously, over glacial cycles, the difference between observed ε_p and that predicted by diffusive models is correlated to $[CO_2]$ (Badger et al. 2019, Stoll et al. 2019).

Recent insights in coccolithophorid physiology may provide some explanations for the observed deviations from the expected physical diffusive model. One factor contributing to the deviations may be that the relationship between ε_p and $[CO_2]$ in alkenone producers is affected by the operation of carbon concentrating mechanisms (CCMs), which enhance the intracellular concentration of CO_2 at the site of photosynthesis when $[CO_2]$ is limiting (Stoll et al. 2019). CCMs have been shown to affect the relationship between ε_p and $[CO_2]$ in other marine phytoplankton (e.g., Hopkinson et al. 2011, Laws et al. 1995). In addition, the ε_f maximum fractionation in Rubisco from diatoms and coccolithophorid *Emiliania huxleyi* has been estimated in vitro to be in the range of 11‰ to 18‰ (Boller et al. 2011, Wilkes et al. 2018), substantially less than the 25‰ to 28‰ routinely used in the calculation of the diffusive model (Pagani 2002, Rau et al. 1996) or the *b* approximation of Equation 5. While most recent multicompartment cellular physical models of carbon isotope fractionation in coccolithophores have accounted for CCMs, none have yet incorporated the potential for the estimated lower in vitro Rubisco fractionation (Bolton & Stoll 2013, Holtz et al. 2017, McClelland et al. 2017). The implications of this lower Rubisco fractionation factor for the phytoplankton proxy, and the potential for other fractionating steps to contribute to observed in vivo fractionation, are still under discussion (Wilkes & Pearson 2019).

One approach to overcome some of the challenges evident in late Quaternary proxy versus ice core comparisons has been to work within the framework of the physical diffusive model to improve constraints for the physiological parameter b. According to the physical diffusive model, b is most sensitive to cell size, algal growth rate, and cell membrane permeability to CO_2, whereas abiotic factors such as ocean temperature, pH, and salinity exert only a minor influence on b (Zhang et al. 2020). Recent determinations of cell membrane permeability to CO_2 in coccolithophore *E. huxleyi* and *Calcidiscus leptoporus* indicate it is not strongly sensitive to environmental factors (Blanco-Ameijeiras et al. 2020). Therefore, cell size and growth rate are expected to most strongly influence b in the case of diffusive CO_2 acquisition. Based on the evidence that coccolithophore cell size correlates inversely with growth rates in all available cultures (Aloisi 2015), one can estimate a combined growth rate and size effect on ε_p (Zhang et al. 2020). This is inferred to be an extension of the size rule proposed to describe growth rates across a range of phytoplankton from picoplankton to large diatoms (Chen & Liu 2010, Finkel et al. 2010). In turn, past cell sizes of alkenone producers can be reconstructed from well-established relationships between cell size and the length of the coccoliths from alkenone producers preserved in the same sediments from which alkenones are extracted (Henderiks & Pagani 2007).

As the physical models of fractionation are under revision, an alternative approach has been to derive a purely empirical estimation of the sensitivity of ε_p to $[CO_2]$ and other environmental variables via assimilation of all published data from laboratory cultures. In this approach, the derived relationship is not dependent on particular assumptions about the mechanism of carbon fixation in coccolithophores (e.g., diffusive versus strongly influenced by CCM) or the Rubisco fractionation factor. This empirical multivariate linear regression model suggests that the relationship between $[CO_2]$ and ε_p is logarithmic rather than hyperbolic, which yields a lower sensitivity of ε_p to $[CO_2]$ in the low CO_2 range (Stoll et al. 2019). This regression analysis suggests that light, growth rate, and cell size will exert secondary effects on ε_p. The observed sensitivity of ε_p to $[CO_2]$ over glacial-interglacial cycles at sites where secondary influences are expected to be minor also fits this relationship well. The Western Caribbean (Badger et al. 2019) and Western Tropical Atlantic (Gonzalez et al., submitted article) and Pacific Warm Pool (Phelps et al., submitted article) all show slopes of ε_p to $[CO_2]$ that are statistically indistinguishable from the slope inferred in laboratory cultures.

In the next section, we review the current best approaches to reconstruct CO_2 from the phytoplankton proxy.

3.2. Current Best Estimates of ε_P-Derived CO_2 Since the Mid-Miocene

The original alkenone-based CO_2 estimates of the late Miocene (Pagani et al. 1999) are quite low compared to other proxies (Foster et al. 2012, Kürschner et al. 2008, Sosdian et al. 2018). Part of the explanation lies in the use of diagenetically altered foraminifera to obtain $\delta^{18}O$-derived temperatures (which are required for calculation of atmospheric CO_2 from dissolved $[CO_2]$) and uncertain partitioning of foraminiferal $\delta^{18}O$ into ice volume and temperature components (Pagani et al. 2010). Super et al. (2018) find substantially higher CO_2 using $U^{k'}_{37}$- and TEX_{86}-derived temperatures. However, new insights into ε_p sensitivity to CO_2 in the recent past are also now available from multiple oligotrophic subtropical locations spanning the ice core CO_2 record, providing a new reference point for the interpretation of ε_p at these locations in the late Neogene. Specifically, the overall low sensitivity of ε_p to glacial-interglacial CO_2 changes implies that the limited variation in ε_p observed in these sites over the past 10 Ma is consistent with a greater variation in CO_2 than previously interpreted (Pagani et al. 1999). Consequently, regardless of whether classic diffusive-based models or empirical culture-based models are used,

tuning of model parameters to match the amplitude of glacial-interglacial CO_2 cycles at these locations results in estimates of significant CO_2 decline in the past 10 Ma, as discussed further below.

Common to all calculation approaches for alkenone-$\delta^{13}C$-based CO_2 is the need to estimate the aggregate growth rate and light effects on ε_p in order to calculate an absolute $[CO_2]$ and atmospheric CO_2 concentration. The simplest and most widespread approach to account for the secondary influences is to assume that they have remained constant at a given oceanographic setting in the past. Such an assumption is most reasonable in subtropical oligotrophic regions far from oceanographic fronts and upwelling systems (**Figure 1**). Higher temperatures increase growth rate, with similar responses observed in field, remotely sensed, and culture data sets (Sherman et al. 2016). However, the temperature stimulation of growth rate is weaker at higher absolute temperatures, which serves to limit variations of growth rate in tropical oligotrophic settings. For example, in the range of surface ocean temperatures in the Western Tropical Atlantic over late Quaternary glacial cycles, temperature-predicted growth rate variation is small and has no correlation with the non-CO_2 variation in ε_p.

For sites in which the secondary influences on ε_p are expected to be nearly constant over time, estimation of the magnitude of these secondary effects is most simply made by late Quaternary anchoring, echoing aspects of the approach of Jasper & Hayes (1990). For this, ε_p is determined in late Quaternary sediments of multiple ages that encompass a range of atmospheric CO_2 concentrations independently constrained from ice core measurements. From the ice core CO_2, the surface ocean $[CO_2]$ for each sample is estimated assuming that the surface ocean CO_2 has remained in equilibrium with the atmosphere at that site, a reasonable assumption for these tropical oligotrophic settings. Because to date there is no approach to segregate the effect of light and growth rate on ε_p in natural ocean settings, the empirical culture regression is simplified to encompass all non-CO_2 influences on ε_p in the intercept (I):

$$\varepsilon_p = m\left(\ln\left[CO_2\right]\right) + I, \qquad\qquad 6.$$

where m is the slope of dependence of ε_p on $[CO_2]$. Because these tropical oligotrophic sites show a sensitivity of ε_p to $[CO_2]$ that is statistically indistinguishable from that in the culture regression, we assume that m has the same value and uncertainty as in the culture study by Stoll et al. (2019) and solve for the late Quaternary I value for each location. The resulting estimations for three sites in tropical oligotrophic gyres—Western Caribbean (ODP 999), Western Subtropical Atlantic (ODP 925), and Western Tropical Pacific (ODP 806)—are shown in **Figure 4e**. These sites are in the warmest parts of the ocean, in which the low solubility of CO_2 maintains $[CO_2]$ (and ε_p) within the range of the culture calibration data set through the Miocene to present. This estimation of CO_2 shows a pronounced decline in average CO_2 over the past 5 Ma, from an average of 320 ppm in the 4.5–5.5 Ma time window to average reconstructed CO_2 of 200 in the 0–0.5 Ma time window (**Figure 4**). Although the data density is lower, there is also a decline in average CO_2 levels over the past 14 Ma. Alternatively, when a diffusive model with traditional parameterization ($\varepsilon_f = 25‰$) is applied to tropical sites such as 925 and 806 over this time interval, much lower and relatively constant CO_2 is inferred. In contrast, when diffusive models are tuned to match the observed glacial-interglacial ε_p sensitivity at these sites by either a lower ε_f (15–18‰) or a systematic dependence of growth rate on $[CO_2]$, calculated amplitudes of CO_2 change since the Miocene are similar to those calculated with the ε_p sensitivity derived from laboratory culture using Equation 6.

An alternative calculation is produced by using the physical diffusive model approximation of Equation 5 and applying a regression between coccolith size and growth rate and therefore

b described by Zhang et al. (2020). This approach can be applied only to sites where both ε_p and coccolith size have been determined. The CO_2 concentrations calculated in this approach resemble the ice core data of the late Pleistocene and, over the past 10 Myr, are lower than the original reported values (Zhang et al. 2013, 2017). A decreasing trend of CO_2 is evident in the most recent 5 Myr, similar to the Quaternary anchoring approach described above, and largely driven by the decline of ε_p over time.

Currently, both approaches are empirical approximations, as neither Equation 5 nor Equation 6, nor the diffusive model of Rau et al. (1996), fully reflect the underlying biological processes of carbon uptake and intracellular conversion and carbon concentration. The next generation of cellular models—featuring updated constraints on the key biological processes such as HCO_3^- pumping and cell membrane permeability to CO_2, accurate fractionation factors for Rubisco and other key unidirectional reactions, and modeling of effects of light on fractionation—may help elucidate which of these approximations are most appropriate and robust. Further research is also required to develop proxy-based indicators of changes in secondary influences (growth rate, light) on ε_p, so that their influences are not mistakenly attributed to variation in $[CO_2]$.

3.3. Current Best Estimates of ε_p-Derived CO_2 in the Eocene to Early Miocene

Reconstruction of CO_2 from alkenones in older sediments is more challenging for several reasons. Alkenone abundance in sediments diminishes, and few sites contain alkenones in quantities sufficient for compound-specific isotopic determinations in sediments older than the late Eocene. The $[CO_2]$ estimated from ε_p are beyond the range covered by existing multivariate linear culture calibrations (Stoll et al. 2019), so empirical relationships for CO_2 sensitivity to ε_p are also lacking. Diffusive models that fit well with the late Quaternary glacial-interglacial cycles—i.e., those using ε_f in the range of 15 to 18—cannot be applied to interpret the Oligocene and older ε_p, which range from 18‰ to 24‰. This suggests either that tuning of ε_f is not the mechanistically correct solution for the late Quaternary or that some facet of phytoplankton carbon fixation or surface ocean production was appreciably different and may require alternative parameterizations or model frameworks. The estimation of the magnitude of secondary growth rate and light effects is especially challenging in older time intervals. The original approaches for estimating the growth rate effect on ε_p, via correlations of *b* with PO_4 and assumption of constant PO_4 or use of model-derived PO_4, are not supported by recent analysis in the late Quaternary (Stoll et al. 2019, Zhang et al. 2019) and Pliocene (Badger et al. 2019). Recent well-calibrated micropaleontological approaches for growth rate estimation from foraminiferal abundance or isotopic gradients (Hernandez-Almeida et al. 2020) are more difficult to apply to extinct taxa whose habitat is not independently constrained and have not yet been implemented.

An alternative approach to obtain the physiological constraints of these ancient alkenone producers is to use the cell size (coccolith length)–growth rate relationship to provide constraints to the *b* parameter (Zhang et al. 2020). For example, the Eocene–Oligocene data set of Pagani et al. (2011) contains both ε_p and surveys of the haptophyte biometry. Zhang et al. (2020) recalculated CO_2, with the caveat that the cell membrane permeability of these extinct species cannot be directly determined; therefore, the calculated Pleistocene value was used. The new results provide more spatially homogeneous estimations of CO_2 and suggest a greater than two-fold drop in CO_2 from the late Eocene to the early Miocene, with a notable decline at the Eocene–Oligocene boundary (**Figure 4**).

4. BORON ISOTOPE-BASED pH AND CO$_2$ RECONSTRUCTIONS

4.1. The δ^{11}B-pH Proxy

Boron isotope-based CO$_2$ reconstructions take advantage of the relationship between the boron isotope composition (δ^{11}B) of marine carbonates and seawater pH. This is grounded in inorganic acid-base and isotopic equilibrium: Boron in seawater is made up of boric acid and borate ion; the proportions of these molecules change with seawater pH, and they exhibit an equilibrium isotope fractionation (Klochko et al. 2006, Nir et al. 2015). Thus, for a given δ^{11}B of total boron in seawater (Foster et al. 2010), the isotopic composition of each boron species is, by mass balance, a function of pH (see **Supplemental Figure 3**). As marine carbonates predominantly incorporate the borate ion (Branson et al. 2016, Rae et al. 2011), their composition is also pH dependent (Hemming & Hanson 1992, Jurikova et al. 2019, McCulloch et al. 2012, Sanyal et al. 1996). pH is a sensitive measure of seawater's CO$_2$ chemistry (**Figures 1** and **3**), allowing δ^{11}B of fossil carbonates to constrain paleo-CO$_2$ (Foster 2008, Hönisch & Hemming 2005).

This inorganic underpinning provides a helpful foundation for the δ^{11}B proxy, but the calculation of pH and CO$_2$ still involves a series of steps and challenges. We discuss these below, in the context of providing an updated composite record of Cenozoic pH and CO$_2$ change from δ^{11}B, and refer readers interested in more detailed discussion of boron isotope systematics to several recent reviews (Branson 2018, Foster & Rae 2016, Hönisch et al. 2019, Rae 2018). Our purpose here is to explore this proxy in ways that can be applied consistently across different studies at the Cenozoic scale. We hope this will provide a useful synoptic view of the scope of boron-based pH and CO$_2$ estimates. However, extra constraints are, in some cases, available from the original studies, and there remains a need to compile and re-evaluate these records—and their uncertainties—more thoroughly (and indeed to generate more data), so we encourage the interested reader to review the original publications and to keep an eye on future developments in this field.

4.2. Updated pH and CO$_2$ Records from δ^{11}B

Here we compile published boron isotope records from the past 66 million years. While δ^{11}B-based CO$_2$ system reconstructions have been made on a variety of calcifiers, our focus here is subtropical planktic foraminifera (Henehan et al. 2013, 2016a; Raitzsch et al. 2018; Sanyal et al. 2001), which occupy surface water environments close to CO$_2$ equilibrium with the atmosphere and are abundant in marine sediment cores, allowing CO$_2$ reconstruction through the Cenozoic (Anagnostou et al. 2016, Pearson & Palmer 2000, Sosdian et al. 2018).

4.2.1. Measured δ^{11}B to δ^{11}B of borate.
We focus on data sets where reproducibility is well demonstrated and supported by later studies: For instance, while the pioneering records of Pearson & Palmer (1999, 2000) laid the groundwork for long-term pH and CO$_2$ reconstruction, the absolute values and temporal evolution of their δ^{11}B data are increasingly at odds with more recent studies in which analytical accuracy and precision are better established. Indeed, even in the past 8 years, interlaboratory reproducibility has improved by a factor of four (compare Stewart et al. 2020 and Gutjahr et al. 2020 to Foster et al. 2013), which should be borne in mind when evaluating some early studies.

Although planktic foraminifera have δ^{11}B values close to that of borate ion, microenvironmental modification results in minor offsets (vital effects), which are corrected for using species-specific calibrations (Henehan et al. 2013, 2016a; Sanyal et al. 2001) (for discussion of approaches in extinct species, see Anagnostou et al. 2016 and Henehan et al. 2020). We largely follow the choices made in the original publications, which also helps account for analytical offsets between negative

thermal ionization mass spectrometry and later multi-collector inductively coupled plasma mass spectrometry measurements. In some cases calibrations have seen minor updates with new data since publication of the original records [for instance, the *Trilobatus sacculifer/Trilobatus trilobus* calibration of Sanyal et al. (2001) has been added to with recent core-top measurements (see Sosdian et al. 2018)], and we incorporate the correction of Greenop et al. (2019) for the influence of changing $\delta^{11}B$ of seawater (see below). The resulting $\delta^{11}B$ of borate is shown in **Figure 5b**. This provides a presentation of $\delta^{11}B$ data that remains close to the measured values, while correcting for species-specific offsets—equivalent to the typical presentation of foraminiferal $\delta^{18}O$ or $\delta^{13}C$. Despite the variety of sites and species used across different studies, the data are remarkably consistent, suggesting that local influences are relatively minor. The overall structure of these boron isotope data shows a close correspondence to compiled benthic $\delta^{18}O$ (Westerhold et al. 2020). As $\delta^{18}O$ tracks global climate (via temperature and ice volume) while $\delta^{11}B$ is primarily sensitive to the CO_2 system, these data, in their raw form, provide a first-order demonstration of the coupling between CO_2 and climate.

4.2.2. $\delta^{11}B$ of borate to pH. To convert $\delta^{11}B$ of borate to pH requires determination of the equilibrium constant of boric acid (K_B) (Dickson 1990) and constraints on $\delta^{11}B$ of seawater ($\delta^{11}B_{SW}$).

4.2.2.1. K_B equilibrium constant. K_B is a function of temperature, salinity, pressure, and the major ion composition of seawater. The influences of salinity and pressure are negligible over plausible ranges in the subtropical surface ocean environments of these cores [e.g., ±1-psu salinity changes $\delta^{11}B$-derived pH by less than 0.005; a ±50-m change in depth of habitat changes pH by less than 0.002 (see Rae 2018)], so for simplicity we assume constant surface pressure and constant salinity of 35 in our $\delta^{11}B$-pH-CO_2 calculations. Temperature has more influence on K_B, although a 5°C change in temperature still changes pH by only 0.06 for a given $\delta^{11}B$. We largely use the temperature reconstructions given in the original publications, which are mainly based on planktic Mg/Ca measurements from the same samples. While it is tempting to try to apply the same style of temperature calibration to all Mg/Ca data, this requires careful evaluation of various secondary influences (e.g., dissolution) considered by the original authors and ideally would incorporate new calibration procedures (e.g., Gray & Evans 2019, Tierney et al. 2019b), which, given the secondary influence of temperature on $\delta^{11}B$-derived pH, is beyond the scope of this review. Finally, we use the MyAMI model (Hain et al. 2015) to account for the influence of changing seawater Ca and Mg concentrations on carbonate system equilibrium constants, with $[Ca^{2+}]$ and $[Mg^{2+}]$ from halite fluid inclusions (Brennan et al. 2013, Horita et al. 2002, Lowenstein et al. 2003, Timofeeff et al. 2006). All codes used in $\delta^{11}B$ calculations are available as a GitHub release.

4.2.2.2. $\delta^{11}B$ of seawater. Boron has an ~10-Myr residence time in seawater, so its isotopic composition may change on multimillion-year timescales (Lemarchand et al. 2000). Here we provide a simple combination of the constraints on $\delta^{11}B_{SW}$ currently available, as shown in **Figure 5c** and outlined below. Given the substantial uncertainty on current $\delta^{11}B_{SW}$ estimates and the long residence time of boron in seawater, which means that any changes should be gradual, our aim is to allow the more precisely measured carbonate $\delta^{11}B$ values to drive the structure of the resulting pH records, rather than assumptions of $\delta^{11}B_{SW}$. Nonetheless, we stress that improving reconstructions of $\delta^{11}B_{SW}$ remains a crucial goal for improving absolute estimates of pH and CO_2.

It is unlikely there has been substantial change in $\delta^{11}B_{SW}$ in the past 5 Myr; some estimates suggest a slight increase (Greenop et al. 2017) and others a slight decrease (Lemarchand et al. 2000), so for simplicity here we use the modern value. Beyond ~5 Ma, all estimates suggest a

decrease in $\delta^{11}B_{SW}$, and changes are also seen in other seawater stable isotope records with shared controls, including δ^7Li, $\delta^{26}Mg$, and $\delta^{44}Ca$ (Akhtar et al. 2020, Misra & Froelich 2012, Pogge von Strandmann et al. 2014). Greenop et al. (2017) use surface to deep ocean gradients in $\delta^{13}C$ to infer pH gradients, over which they measure $\delta^{11}B$ to solve for $\delta^{11}B_{SW}$. The Lemarchand et al. (2000)
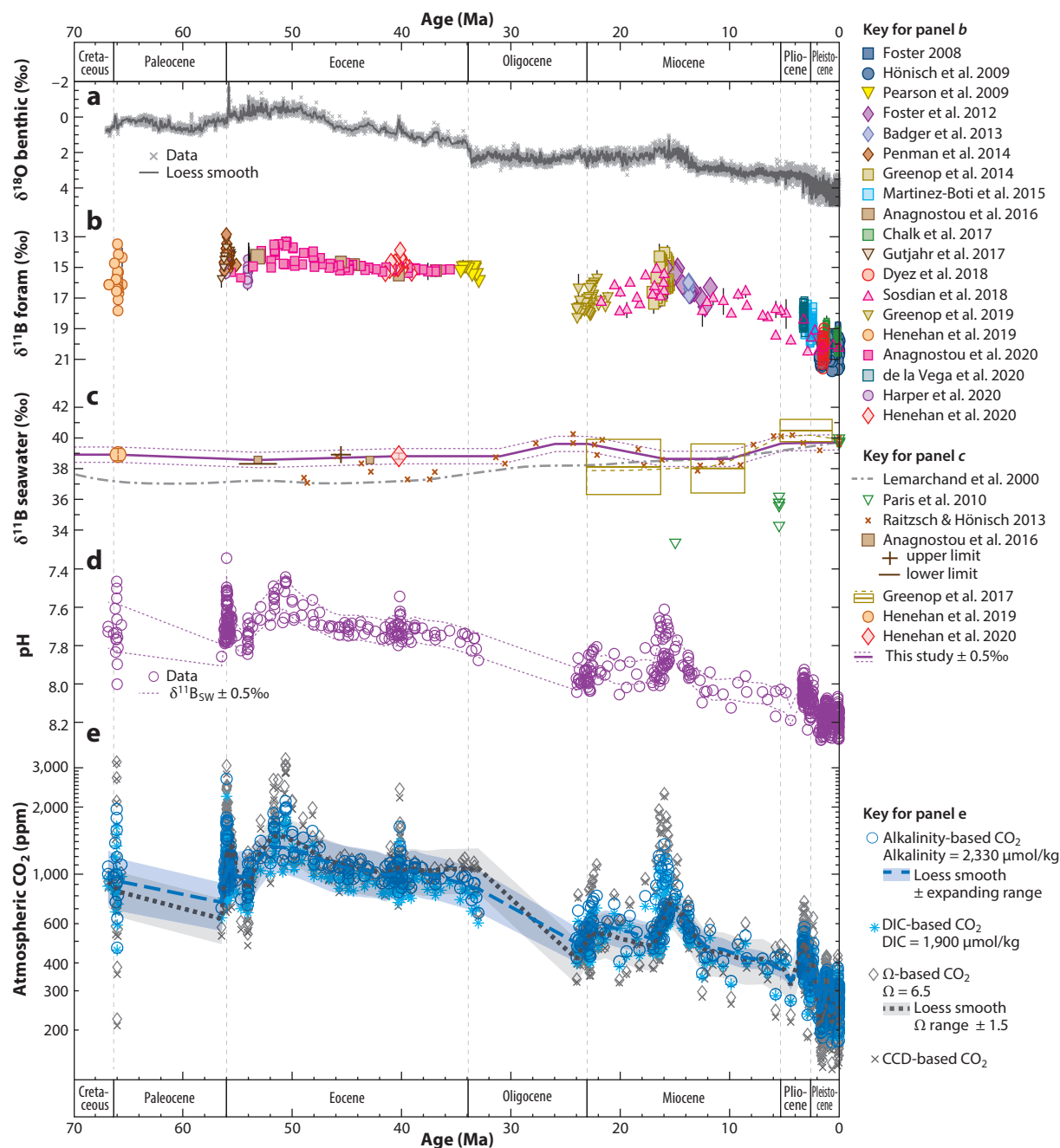
(*Caption appears on following page*)

Figure 5 (*Figure appears on preceding page*)

Boron isotope-derived estimates of pH and CO_2. (*a*) Benthic $\delta^{18}O$ from Westerhold et al. (2020). (*b*) $\delta^{11}B$ on planktic foraminifera corrected for vital effects to give $\delta^{11}B$ of borate (*colored symbols*, given by study—see legend), which tracks the CO_2 system, although with influence from $\delta^{11}B_{SW}$. Note that uncertainties on $\delta^{11}B$ measurements are shown but in most cases are smaller than the symbols. (*c*) Estimates of seawater boron isotope composition by study (see legend). Note that the ± 0.5‰ band is intended for illustration (see panel *d*)—assessing the true uncertainty of $\delta^{11}B_{SW}$ over the Cenozoic is beyond the scope of this study. The scale in panel *c* is equivalent to the scale in panel *b* to aid comparison. (*d*) pH, calculated from $\delta^{11}B$ of borate in panel *b* and $\delta^{11}B_{SW}$ in panel *c*, along with K_B estimates accounting for changes in temperature and major ion composition (see Section 4.2.2). (*e*) Atmospheric CO_2 calculated from pH in panel *d* using four different approaches (see legend and discussion in Section 4.2.3). Comparison of panels *b*, *d*, and *e* illustrates that the main influence on reconstructed pH and CO_2 is measured $\delta^{11}B$, rather than secondary corrections. At each stage, boron isotope data share similar structure with $\delta^{18}O$, indicating first-order coupling between CO_2 and global climate. Abbreviations: CCD, carbonate compensation depth; DIC, dissolved inorganic carbon. Boron isotope data are from Anagnostou et al. (2016, 2020), Badger et al. (2013), Chalk et al. (2017), de la Vega et al. (2020), Dyez et al. (2018), Foster (2008), Foster et al. (2012), Greenop et al. (2014, 2017, 2019), Gutjahr et al. (2017), Harper et al. (2020), Henehan et al. (2019, 2020), Hönisch et al. (2009), Lemarchand et al. (2000), Martínez-Botí et al. (2015), Paris et al. (2010), Pearson et al. (2009), Penman et al. (2014), Raitzsch & Hönisch (2013), and Sosdian et al. (2018). All data are available as online **Supplemental Material**.

$\delta^{11}B_{SW}$ model also declines around this time, although less steeply than the Greenop et al. (2017) central estimate; here we use the average of these estimates until 10 Ma and then maintain this value until 16 Ma. In the early Miocene to Oligocene, the only available data-based estimate of $\delta^{11}B_{SW}$ is by Raitzsch & Hönisch (2013), based on benthic $\delta^{11}B$ measurements and an assumption of gradual change in deep ocean pH. Ideally, $\delta^{11}B_{SW}$ estimates would be free from assumptions of long-term pH change, as reconstructing pH is our ultimate goal. However, in the absence of other constraints, we follow the Raitzsch & Hönisch (2013) estimates in this window. Beyond this, Anagnostou et al. (2016) provide an estimate of $\delta^{11}B_{SW}$ for the Eocene, using constraints from planktic foraminiferal species with habitat depths spanning a range of pH (as pioneered in Palmer et al. 1998) and conservative assumptions based on carbonate saturation and oxygen gradients. Henehan et al. (2019, 2020) also follow this approach and provide upper and lower limits on $\delta^{11}B_{SW}$ at the Cretaceous–Paleogene (KPg) boundary and an updated estimate for the middle Eocene.

Combining $\delta^{11}B$ of borate, K_B, and $\delta^{11}B_{SW}$, and using the $\delta^{11}B$ to pH relationship of Rae (2018), yields the reconstruction of pH shown in **Figure 5d**. As with $\delta^{11}B$ of borate, this record closely tracks $\delta^{18}O$, again supporting the long-term coupling of the ocean-atmosphere CO_2 system and climate. While the absolute pH values we reconstruct are contingent on improved estimates of $\delta^{11}B_{SW}$ (see **Figure 5d**), the structure of the record will be predominantly driven by changes in seawater pH.

4.2.3. pH to CO_2.
Calculation of CO_2 from pH requires constraints on one other parameter of the ocean carbonate system. Here we explore variants of common approaches based on constraints from alkalinity, carbonate saturation, and the carbonate compensation depth (CCD). We briefly describe these approaches below and then discuss their implications, strengths, and weaknesses in Section 4.3. Our calculations account for changing $[Ca^{2+}]$ and $[Mg^{2+}]$ (Hain et al. 2015) and are done in a modified version of csys.m (Zeebe & Wolf-Gladow 2001), which gives identical values to CO2SYS.m (van Heuven et al. 2009) and seacarb (Gattuso et al. 2015a), and has flexibility to explore a range of input parameters (available on GitHub).

4.2.3.1. Alkalinity (or dissolved inorganic carbon).
Studies focused on the past $\sim$5 million years have typically assumed a range of alkalinity values, which can be combined with pH to yield relatively precise estimates of CO_2 (see **Supplemental Figure 4**; Section 4.3). Here we use a central value of 2,330 µmol/kg with a range of ± 175 µmol/kg for the past 5 Ma (following

Martínez-Botí et al. 2015), which is large compared to the ± 96-μmol/kg range found in modern subtropical waters (**Supplemental Figure 1**). We expand this range to ± 350 at 15 Ma and ± 600 at 50 Ma, guided by results from models that explore a wide range of carbon cycle parameter space; for instance, Greene et al. (2019) find alkalinity values of $\sim$1,400 to 2,600 in cGENIE system model experiments where outgassing rate changes by a factor of $\sim$2.5, weathering rate doubles, and CO_2 varies from $\sim$280 to 2,100 ppm. A similar range of around ± 600 is found in approaches combining ε_p-derived CO_2 and constraints from the CCD (Boudreau et al. 2019, Zeebe & Tyrrell 2019). For illustration we also show a CO_2 estimate based on pH and constant DIC (**Figure 5e**).

4.2.3.2. Calcite saturation state. On long timescales alkalinity may evolve, so it is useful to look for further constraints on the carbonate system. The saturation state of calcite (Ω; see **Figure 1**) can add value, in that it is regulated by carbonate compensation (Broecker & Peng 1987, Sarmiento & Gruber 2006, Zeebe 2012). Put simply, if Ω drops, $CaCO_3$ on the deep sea floor will dissolve and the supply of alkalinity to the ocean by weathering will exceed its removal by $CaCO_3$ burial, leading alkalinity to rise and Ω to increase back up; if Ω rises, more carbonate may precipitate or be buried, drawing alkalinity and Ω back down. Thus, Ω tends to stay within a relatively limited range of values on long timescales in carbon cycle models with pelagic carbonate [e.g., ± 0.8 in Ridgwell (2005), ± 0.5 in Hönisch et al. (2012), ± 0.7 in Boudreau et al. (2019)]. Here we show a CO_2 reconstruction assuming Ω of 6.5 ± 1.5 (following Anagnostou et al. 2016); note that these values are intended to characterize the subtropical sites used in these reconstructions, so Ω is elevated compared to global surface ocean estimates (Boudreau et al. 2019, Ridgwell 2005, Takahashi et al. 2014) (**Supplemental Figure 1**). Ω is combined with calcium concentration from fluid inclusions and K_{SP} (calculated as a function of the T, S, P, Ca^{2+}, and Mg^{2+} conditions described in Section 4.2.2.1) to give $[CO_3^{2-}]$, which is then combined with pH to calculate CO_2 (**Figure 5e**).

4.2.3.3. Carbonate compensation depth. Further insight may be gained from the CCD (Boudreau et al. 2019, box 1; Tyrrell & Zeebe 2004; Zeebe & Tyrrell 2019) to account for potential changes in ocean saturation state over time. In brief, these approaches assume that the depth of the sedimentary CCD is known and is related to the onset of undersaturated conditions in the overlying waters (see **Figure 1**). Tyrrell & Zeebe (2004) and Zeebe & Tyrrell (2019) then use estimates of $[Ca^{2+}]$ to calculate $[CO_3^{2-}]$ at this water depth and an assumption of deep to surface ocean $[CO_3^{2-}]$ gradient to obtain $[CO_3^{2-}]$ in surface waters. Here we use Zeebe & Tyrrell's (2019) recently updated $[CO_3^{2-}]$ estimate, scaled for subtropical surface sites with modern $[CO_3^{2-}]$ of 275 μmol/kg, in combination with δ^{11}B-derived pH to calculate CO_2 (**Figure 5e**).

4.3. Evaluating δ^{11}B-Based CO_2 System Reconstructions

For a given δ^{11}B-derived pH, each of the second carbonate system parameter scenarios described above yields broadly similar CO_2 (**Figure 5e**). In particular, values from the alkalinity and DIC scenarios are closely grouped, as are values using the CCD and Ω. As pointed out by Zeebe & Tyrrell (2019), the largest driver of their change in $[CO_3^{2-}]$ is the halving of $[Ca^{2+}]$ over the Cenozoic, which by itself changes $[CO_3^{2-}]$ by a factor of two; the $\sim$25% change in CCD depth has less impact. Furthermore, the CCD estimate used by these authors is relatively smooth and thus introduces relatively little extra structure to the $[CO_3^{2-}]$ estimate beyond that driven by the long-term increase in $[Ca^{2+}]$ (see **Supplemental Figure 5**).

Each of these approaches has strengths and weaknesses. The attraction of the Ω or CCD approach is its physical and observational basis: Carbonate compensation is self-regulating, and $CaCO_3$ has persisted in deep sea sediments since the advent of pelagic carbonate production without ever blanketing the ocean abyss (Boudreau et al. 2019, Ridgwell 2005, Tyrrell & Zeebe 2004).

However, $[Ca^{2+}]$ is a critical input to these calculations, and its absolute values are relatively poorly known. Current estimates are based on halite fluid inclusions (Brennan et al. 2013, Horita et al. 2002, Lowenstein et al. 2003, Timofeeff et al. 2006), but because gypsum ($CaSO_4$) precipitates before halite in evaporite systems (and as there is an excess of SO_4^{2-} in Cenozoic seawater compared to Ca^{2+}), Cenozoic halite inclusions contain no calcium. Reconstructing $[Ca^{2+}]$ requires an assumption of the $[Ca^{2+}] \times [SO_4^{2-}]$ product (see Brennan et al. 2013, Broecker 2013), which is assigned a range spanning 0.5 to 1.5 times the modern value, resulting in uncertainty of around 30% on estimates of $[CO_3^{2-}]$ (see **Supplemental Figure 5**).

Reconstructing the CCD is also challenging, ideally requiring global, depth-resolved $CaCO_3$ data, from settings with relatively constant export productivity (Palike et al. 2012) and well-constrained subsidence histories (Campbell et al. 2018). Furthermore, the CCD can be decoupled from saturation state in the overlying seawater (Boudreau et al. 2010, Greene et al. 2019), and the gradient in $[CO_3^{2-}]$ between the depth of the CCD and the ocean surface is also uncertain (see discussion in Zeebe & Tyrrell 2019).

Most critically, perhaps, for pH-based CO_2 reconstructions is that pH and $[CO_3^{2-}]$ make a relatively unstable pairing for determining the carbonate system. As illustrated in **Supplemental Figure 4**, variable pH with stable $[CO_3^{2-}]$ necessitates large and closely coupled fluctuations in alkalinity and DIC. Although this might be partially achieved through carbonate compensation and weathering feedbacks, it is hard to envision these processes matching the size and tempo of the required alkalinity and DIC change.

Alkalinity provides a more stable pairing with pH for CO_2 system determination and results in coupled changes in pH, CO_2, and $[CO_3^{2-}]$ driven by modest changes in DIC (see **Supplemental Figures 4** and **5**). A constant DIC scenario gives similar results but with muted changes in alkalinity instead, and as alkalinity is generally more stable in the modern surface ocean than DIC (being influenced by fewer processes), its use is preferable. The drawback of using alkalinity is that it lacks self-regulation or direct observational constraints. However, even a wide range of possible alkalinity values yield well-constrained CO_2 estimates if paired with relatively precise estimates of pH, an approach borne out by alkalinity-derived pH-CO_2 reconstructions that fall within ± 25 ppm of ice core values on glacial-interglacial timescales (e.g., Chalk et al. 2017, Hain et al. 2018, Rae 2018).

Our favored scenario thus draws on the strengths of each of these approaches, by using alkalinity with $\delta^{11}B$-derived pH in our CO_2 system calculations, and checking that the resulting saturation state falls within reasonable bounds. For our central alkalinity estimate, we find Ω values that fall within a range of ~ 5 to 8 (**Supplemental Figure 5**), similar to the ranges considered reasonable in previous studies (e.g., Anagnostou et al. 2016). This calculation also allows for excursions in Ω, which we find align (**Supplemental Figure 5**) with times of widespread carbonate dissolution, such as the Paleocene–Eocene Thermal Maximum (PETM) (Zachos et al. 2008), or oversaturation, such as the aftermath of the KPg extinction (Henehan et al. 2016b). We note that for different time intervals or applications, other approaches may be more appropriate, and that some studies have found extra constraints within specific intervals (e.g., Sosdian et al. 2018), and we encourage continued efforts with Earth system models to explore plausible scenarios within carbonate system space on a range of different timescales. However, in terms of CO_2 reconstruction, it is important to note that the range of approaches explored here yield broadly similar CO_2 estimates. While a secondary assumption is needed for CO_2 calculation, it is less critical than might be assumed, provided that pH is well-known (Hain et al. 2018, Rae 2018). Indeed, pH provides a valuable constraint on the evolution of the ocean-atmosphere CO_2 system in its own right. The major hurdle to improving absolute pH estimates on long timescales remains $\delta^{11}B_{SW}$, which requires new observational and modeling constraints.

5. TOWARD A CONSISTENT PICTURE OF THE EVOLUTION OF THE CENOZOIC CO_2 SYSTEM

The updated records of CO_2 from alkenones and $\delta^{11}B$ presented here provide a more consistent picture of Cenozoic CO_2 change than in some earlier studies (**Figure 6**). We reconstruct
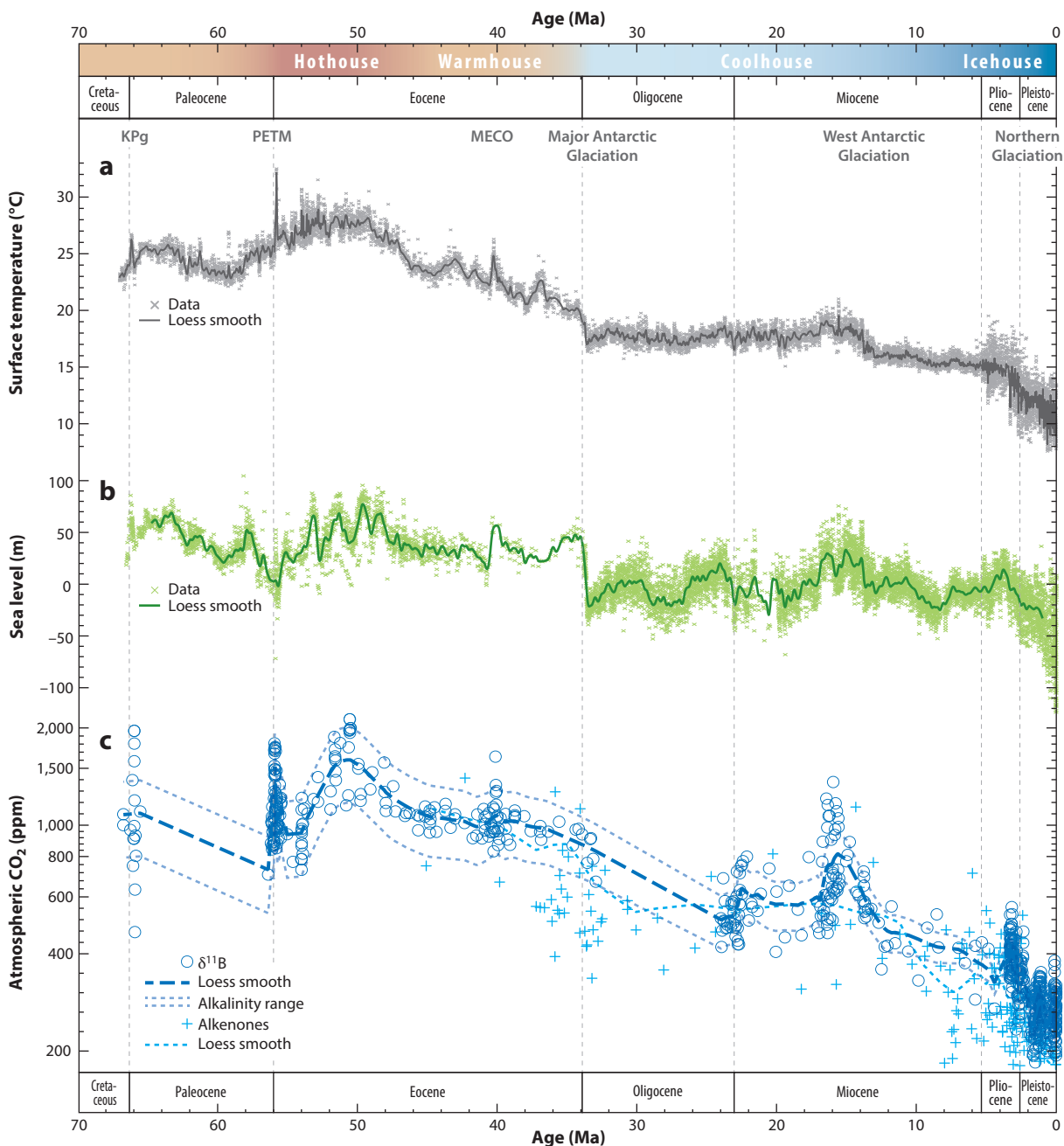
(*Caption appears on following page*)

Figure 6 (*Figure appears on preceding page*)

Cenozoic CO_2 and global climate. (*a*) Surface temperature estimated from the benthic $\delta^{18}O$ stack of Westerhold et al. (2020), using the algorithm of Hansen et al. (2013). (*b*) Sea level estimates from Miller et al. (2020). (*c*) Atmospheric CO_2 reconstructions from boron isotopes (*blue dashed lines* show influence of alkalinity range as in **Figure 5**) and alkenones (using Quaternary anchoring for data younger than 23 Ma, and updated constraints on panel *b* for data older than 23 Ma). Note that in each of these records, more detailed (and coherent) structure is found at shorter timescales—for instance, associated with orbitally paced glacial-interglacial cycles in the late Neogene (Chalk et al. 2017, Hönisch et al. 2009, Martínez-Botí et al. 2015) or rapid carbon cycle perturbations at the Cretaceous–Paleogene (KPg) (Henehan et al. 2019), Paleocene–Eocene Thermal Maximum (PETM) (Gutjahr et al. 2017, Penman et al. 2014), and Middle Eocene Climatic Optimum (MECO) (Henehan et al. 2020). Examples of notable climatic events are listed at the top of the figure along with the climate states of Westerhold et al. (2020). A simplified version of this figure showing CO_2 and benthic $\delta^{18}O$ (without temperature conversion) is shown in **Supplemental Figure 7**. All data are available online as **Supplemental Material**.

atmospheric CO_2 of ∼1,500 ppm in the early Eocene, dropping through the Eocene and at the Eocene–Oligocene boundary to ∼600 ppm in the early Neogene, increasing during the Mid-Miocene Climatic Optimum, and then falling to values of ∼400 ppm during the Pliocene warm period and ∼300–180 ppm during the late Pleistocene ice ages. While each method has uncertainties, these are largely independent, so their broad convergence on similar CO_2 histories is encouraging.

As ε_p and $\delta^{11}B$ provide two independent measures of the carbonate system ($[CO_2]$ and pH), it is tempting to combine them to determine the other carbonate system parameters (e.g., DIC, alkalinity, $[CO_3^{2-}]$, $[HCO_3^-]$). We explore this possibility in **Supplemental Figure 5** and note that the resulting carbonate chemistry stays within reasonable bounds. Different carbonate system components are more or less easily constrained through these pH and $[CO_2]$ data due to the inter-relationships within the carbonate system (see **Supplemental Figure 4**). Carbonate ion concentration, for instance, is closely coupled with pH and $[CO_2]$ (**Figure 2**), so most of the scenarios in **Supplemental Figure 5** constrain $[CO_3^{2-}]$ to within ±50 μmol/kg and show a consistent doubling of carbonate ion concentration over the Cenozoic. Absolute values of alkalinity and DIC will always be harder to constrain with these data pairings, as similar pH, $[CO_2]$, and $[CO_3^{2-}]$ can be found across a wide range of alkalinity and DIC values (see Rae et al. 2011) (**Figure 2**; **Supplemental Figure 4**). However, while the sizes of the alkalinity and DIC inventories are hard to constrain, their ratio is closely coupled with—and indeed determines—pH, $[CO_2]$, and $[CO_3^{2-}]$ and so is constrained relatively precisely. The evolution of the alkalinity to DIC ratio may indeed provide a useful framing for considering causes of Cenozoic CO_2 change.

6. CAUSES OF CO₂ CHANGE

The records of the CO_2 system provided here offer an updated target for efforts to understand the drivers of Cenozoic CO_2 change. To first order, long-term CO_2 change is thought to result from shifts in the balance between carbon release from the planet's interior and its drawdown via silicate weathering (Berner 1991, Isson et al. 2020, Kasting 2019, Kump et al. 2000, Raymo & Ruddiman 1992, Urey 1952). Understanding of these processes, and how they have influenced CO_2 over the Cenozoic, is rapidly evolving (Caves Rugenstein et al. 2019, Misra & Froelich 2012, Torres et al. 2017), and their review is beyond the scope of this contribution. We highlight here a few key features of our records that may help evaluate the drivers of long-term CO_2 change.

We note that of the ∼1,000-ppm CO_2 change over the Cenozoic, ∼200 ppm can be explained by temperature and ∼125 ppm by the shift in the major ion composition of seawater (∼90 ppm from $[Mg^{2+}]$ and ∼35 ppm from $[Ca^{2+}]$) (see **Supplemental Figure 6**). The temperature influence comes about due to changes in the CO_2 system equilibrium constants (**Figure 1**), which increase CO_2's solubility in colder waters (see **Supplemental Figure 1**). This represents a positive

feedback on Cenozoic CO_2 change: As atmospheric CO_2 falls and climate cools, the CO_2 system's equilibrium state will shift to partition more CO_2 into the ocean from the atmosphere. The influence of major ion chemistry also derives from changes to CO_2 system equilibrium constants. The drivers of secular changes in seawater composition are still debated (see Broecker 2013), but several candidates may impact CO_2 both directly and via this equilibrium constant effect: For instance, decreased seafloor spreading may decrease outgassing of volcanic CO_2 and also partition CO_2 from the atmosphere to the ocean by increasing $[Mg^{2+}]$ and decreasing $[Ca^{2+}]$ in seawater.

Accounting for CO_2 changes due to temperature and major ion chemistry leaves $\sim$675 ppm (approximately two-thirds of the total CO_2 change) to be explained by changes in the master variables of the ocean-atmosphere carbonate system: alkalinity and DIC. As discussed in Section 5, although the size of the alkalinity and DIC inventories is hard to constrain, their ratio in surface waters is relatively well determined by our data. CO_2 system change over the Cenozoic is set by an increase in the ratio of alkalinity to DIC, from $\sim$1.1 to 1.25, which may be achieved by relatively subtle shifts in alkalinity supply by weathering relative to DIC supply by outgassing. For instance, a decrease in outgassing over the Cenozoic can be achieved without necessarily requiring a change in the rate of spreading and subduction but through a change in the carbonate content of the subducted slab (Mason et al. 2017) as Tethyan limestones give way to deep Pacific clays (Edmond & Huh 1997). Similarly, an increase in alkalinity supply from weathering may come about by an increase in the efficiency of alkalinity extraction and thus CO_2 drawdown during silicate weathering, driven by increasing erosion rates in the Neogene, with little change in total weathering flux (Caves Rugenstein et al. 2019).

Given the size of potential changes in CO_2 outgassing and weathering fluxes, tight regulation of CO_2 is required to prevent runaway greenhouse or icehouse conditions (Berner & Caldeira 1997, Isson et al. 2020, Penman et al. 2020). The dependence of silicate weathering on CO_2 and climate provides such a feedback (Li et al. 2016), with the ocean carbonate system playing a mediating role: the ocean receives the products of weathering and outgassing and, via this balance of alkalinity and DIC, sets atmospheric CO_2.

7. COUPLING OF CO_2 AND GLOBAL CLIMATE OVER THE PAST 66 MILLION YEARS

> Buffeted about by changes both on the supply side and on the removal side, the CO_2 content of the atmosphere has undergone large changes. These changes have served as the primary driver of Earth's climate.
>
> —Wally Broecker (2015)

The past 66 million years have witnessed a dramatic change in Earth's climate, evolving from the ice-free Hothouse of the early Eocene to the frigid Icehouse of the Last Glacial Maximum (Westerhold et al. 2020, Zachos et al. 2001). Changing levels of atmospheric CO_2 have long been implicated in the well-documented cooling of the climate through the Cenozoic (e.g., Berner et al. 1983, Raymo & Ruddiman 1992); however, outside of a handful of well-studied climate transitions (Foster et al. 2012, Pagani et al. 2011, Pearson et al. 2009), it has been hard to make a close link between CO_2 and climate. Our new combined marine-based CO_2 compilation shows, more clearly than in previous studies, a close correlation between CO_2 and records of global temperature (based on either geochemical reconstructions and/or the state of the cryosphere) through the entire Cenozoic (**Figure 6**). Our CO_2 data are closely tied to the different states of Cenozoic climate (see top of **Figure 6**), as identified by statistical analysis of benthic $\delta^{18}O$ (Westerhold et al. 2020). During the Hothouse of the early Eocene, CO_2 levels are $\sim$1,500 ppm, contributing to

extreme global warmth and, in combination with changing cloud properties, a reduced latitudinal temperature gradient (Evans et al. 2018, Zhu et al. 2019). Falling CO_2 is associated with the cooling to the middle and late Eocene Warmhouse (Anagnostou et al. 2016, Inglis et al. 2015), which has CO_2 levels of ~1,000 ppm (Anagnostou et al. 2020), and CO_2 falls below ~800 ppm at the Eocene–Oligocene boundary, associated with the first major growth of ice on Antarctica (Pearson et al. 2009, Zhang et al. 2020). The Coolhouse climates of the Oligocene and early Miocene are associated with CO_2 of ~600 ppm, although the Oligocene remains a notable data gap for records that can be assessed following the procedures used here (Sections 3 and 4). Antarctic ice loss at the Miocene Climatic Optimum is associated with a peak in CO_2 (Foster et al. 2012, Zhang et al. 2013), and CO_2 falls again during the Miocene Climate Transition as the East Antarctic Ice Sheet stabilizes and the West Antarctic Ice Sheet grows (Sosdian et al. 2018, Stoll et al. 2019). Following a slight rise during the mid-Pliocene Warm Period (de la Vega et al. 2020, Pagani et al. 2010, Seki et al. 2010), CO_2 falls again as the Plio–Pleistocene Icehouse intensifies, including the growth of large Northern Hemisphere ice sheets, with increased variability associated with progressively lower CO_2 levels during glacial maxima and a more gradual decline in interglacial levels (Chalk et al. 2017, Dyez et al. 2018, Hönisch et al. 2009).

These data underscore the importance of CO_2 as the primary control knob of the greenhouse effect and Earth's climate (Lacis et al. 2010) through at least the past 66 million years. CO_2 is, however, unlikely to be the only driver of Cenozoic climate change. For instance, Anagnostou et al. (2016) calculated that around 65% of the warmth of the Eocene was driven by the higher CO_2 of this interval, with the remaining 35% due to changes in other boundary conditions, such as a reduced planetary albedo due to a smaller cryosphere (**Figure 6b**) and altered vegetation distributions. Other secondary drivers of climate over this interval include the position of the continents and an increase in solar constant through time (Lunt et al. 2016).

To further explore the relationship between long-term CO_2 change and climate, we plot estimates of global temperature evolution against CO_2 doublings (**Figure 7**); the slope of this relationship gives a rudimentary form of climate sensitivity, although we stress two important caveats. First, it is crucial to note that estimates of Earth system sensitivity of this type are distinct from equilibrium or Charney sensitivity, most commonly used in relation to future climate change (Sherwood et al. 2020), due to the operation of slow feedbacks in the Earth system, such as changes in land ice (Rohling et al. 2012), and nonclimate system effects, such as changes in paleogeography (e.g., Anagnostou et al. 2016, Farnsworth et al. 2019). Second, the temperature estimates used here are also crude, based on a scaling with benthic $\delta^{18}O$ (Westerhold et al. 2020) following Hansen et al. (2013), and the apparent discontinuities at 5.3 and 34 Ma are synchronous with a change in climate state due to ice growth but also a related change in the scaling function (although we note broad agreement with independent compilations of surface temperature shown in **Figure 7b**). Nonetheless, it is clear, even with these caveats, that atmospheric CO_2 and temperature are closely coupled, both across the data set as a whole and within shorter time windows. While the data set as a whole suggests a relatively high climate sensitivity, much of this temperature change is apparently accomplished by jumps between different climate states. These jumps, if not simply a function of changes in the $\delta^{18}O$-temperature scaling factor, could be linked to changes in Earth's albedo associated with ice growth at these times or other tipping elements, such as changes in cloud properties (e.g., Schneider et al. 2019). The compilation also supports the potential state dependence to climate sensitivity through the Cenozoic noted in other recent studies (Anagnostou et al. 2020, Farnsworth et al. 2019, Zhu et al. 2019), permitting higher values in the Eocene and Plio–Pleistocene and more moderate values in the Miocene. However, given the caveats currently involved in these types of comparisons between CO_2 and global temperature, we encourage further research to continue to explore and refine these relationships.
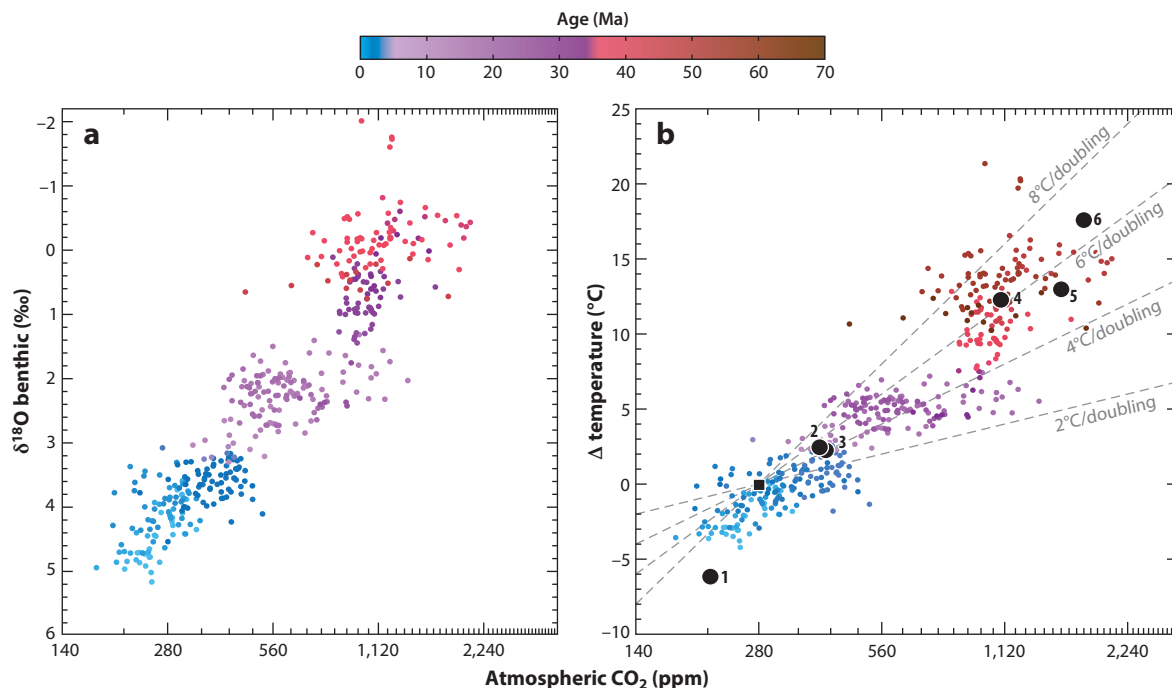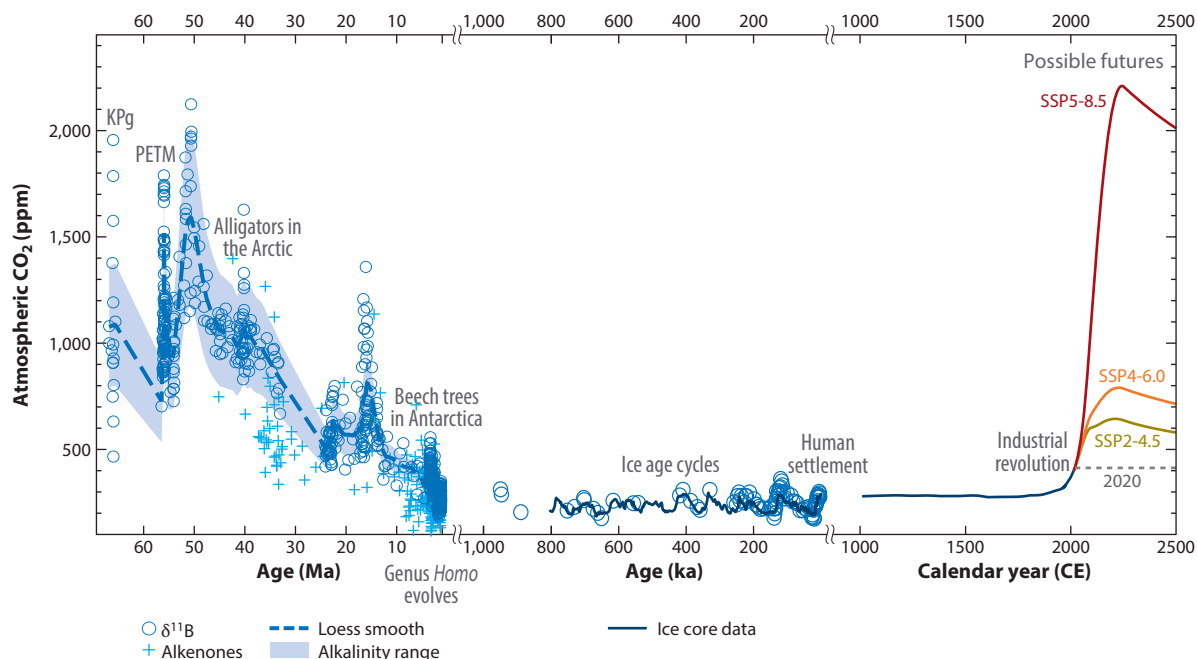
Figure 7

Relationship between CO_2 and climate over the Cenozoic. Atmospheric CO_2 is as plotted in **Figure 6**, binned into 0.01 Myr time windows and shown on a log(2) scale to display CO_2 doublings. Symbol color indicates age, with the breaks in color broadly corresponding to the Hothouse, Warmhouse, Coolhouse, and Icehouse states (**Figure 6**) of Westerhold et al. (2020). Panel *a* shows benthic $\delta^{18}O$ data (Westerhold et al. 2020). Panel *b* shows benthic $\delta^{18}O$ data converted to an estimate of surface temperature change, following Hansen et al. (2013); note that discontinuities at 5.3 and 34 Ma may be in part due to changes in this algorithm. Black circles indicate independent proxy-derived estimates of surface temperature: ❶ Last Glacial Maximum (Tierney et al. 2020b), ❷ Pliocene (de la Vega et al. 2020), ❸ Pliocene (McClymont et al. 2020), ❹ late Paleocene, ❺ Early Eocene Climatic Optimum, and ❻ Paleocene–Eocene Thermal Maximum (Inglis et al. 2020). Dashed lines denote different degrees of temperature change per CO_2 doubling, providing an estimate of Earth system sensitivity.

8. THE PAST AND FUTURE OF CO_2 CHANGE

Over the past 150 years, humans have become a dominant force of change within the Earth system (**Figure 8**). By burning fossil fuels, human society has converted the geological reservoirs most rich in carbon directly into atmospheric CO_2. At the time of writing in 2020, CO_2 is 414 ppm, a level last seen on Earth in the Pliocene around 3 million years ago (**Figure 8**), a time with global temperatures ~3°C warmer than preindustrial, smaller ice sheets, and ~20-m higher sea level (Dutton et al. 2015, McClymont et al. 2020, Raymo et al. 2018). As de la Vega et al. (2020) recently noted, at current rates of CO_2 emission, we are likely to exceed Pliocene-like CO_2 values within the next decade. Given the shape of CO_2 evolution through the Neogene, we are therefore rapidly heading toward levels of CO_2 not seen since the Mid-Miocene Climatic Optimum, 15 million years ago. High emission scenarios, where fossil fuel use continues to grow unabated, illustrate the potential for CO_2 to peak at ~2,200 ppm, exceeding anything seen in the past 66 million years (**Figure 8**). While such high emissions are now considered unlikely [due to anticipated trends toward decreasing coal consumption and less CO_2-intensive energy supply (Hausfather & Peters 2020)], they underscore the potential impact of future energy choices.

Figure 8

Paleo-CO_2 context for future CO_2 change scenarios. Note the breaks in the age axis to allow different timescales to be compared. CO_2 scenarios associated with shared socioeconomic pathways (SSPs) SSP2-4.5, SSP4-6.0, and SSP5-8.5 are from Meinshausen et al. (2019), as used in the Intergovernmental Panel on Climate Change Sixth Assessment Report; scenario numbers refer to the change in radiative forcing in watts per square meter. The 2020 CO_2 level of 414 ppm is from **https://scrippsco2.ucsd.edu**. Paleo-CO_2 data are as plotted in **Figure 6**. Although Earth has experienced elevated CO_2 levels within the past 66 million years, these are associated with a world entirely unfamiliar to our genus, with beech forests growing in parts of Antarctica during the Pliocene (Rees-Owen et al. 2018) and alligators roaming the Arctic during the Eocene (Eberle & Greenwood 2012). Abbreviations: KPg, Cretaceous–Paleogene (boundary extinction); PETM, Paleocene–Eocene Thermal Maximum.

These comparisons put historic and future CO_2 rise into a geological context, although comparing the geological past and our potential future is not straightforward (for more detailed discussions, see Burke et al. 2018 and Tierney et al. 2020a). Geological CO_2 change generally occurs over millennia to millions of years, which allows the climate system to keep pace with changing CO_2 levels (Rohling et al. 2012). The change in climate forcing due to anthropogenic carbon emissions is ~10 times faster than even the most abrupt geological carbon release in the past 66 million years (the PETM) (e.g., Zeebe et al. 2016), with only the meteorite impact at the KPg boundary causing more rapid global change (e.g., Henehan et al. 2019). As a consequence, the climate system is currently far from equilibrium, with equilibration timescales on the order of millennia largely set by the slow responses of the deep ocean and the cryosphere (Rohling et al. 2012). Nonetheless, it remains an important point that only by immediately and substantially cutting carbon emissions will we limit global temperature change and prevent a return to a planetary climate entirely unfamiliar to our genus.

9. OUTLOOK

CO_2 reconstructions from phytoplankton $\delta^{13}C$ and foraminiferal $\delta^{11}B$ have evolved substantially in recent years. Here we have attempted to review Cenozoic CO_2 estimates from these methods

in a consistent framework, informed by the latest understanding of the assumptions underlying these proxies. This reveals an increasingly coherent picture of CO_2 change over the past 66 million years and a close coupling between CO_2 and climate.

Several significant challenges remain in the years ahead. For alkenone-based reconstructions, these include continued uncertainties in understanding of biological mechanism (Rubisco fractionation, CCM and upregulation, physiological evolution) and the need for continued improvement on constraining secondary influences on ε_p (growth rate, light limitation), especially within older time intervals. Further exciting areas for future research include development of realistic physical models of phytoplankton $\delta^{13}C$ and expansion of the proxy into deeper time using other related compounds. For boron isotopes, $\delta^{11}B_{SW}$ remains the most significant uncertainty in absolute pH and CO_2 values on long timescales. Improved efforts to reconstruct and/or model secondary constraints on the carbonate system, including the major ion chemistry of seawater, will also benefit $\delta^{11}B$-based records. In both proxy systems there is also a continued need to increase the temporal and spatial coverage of reconstructions.

However, while uncertainties in each method persist, they are largely independent, so the increasing level of agreement in CO_2 reconstructions from these methods is encouraging. Evaluation of the Cenozoic CO_2 record underscores the truly geological scale of anthropogenic CO_2 change and the urgent need to reduce CO_2 emissions to prevent Earth's future climate from equilibrating to CO_2 levels last seen in its increasingly distant past.

DISCLOSURE STATEMENT

The authors are not aware of any affiliations, memberships, funding, or financial holdings that might be perceived as affecting the objectivity of this review.

ACKNOWLEDGMENTS

LITERATURE CITED

Akhtar AA, Santi LM, Griffiths ML, Becker M, Eagle RA, et al. 2020. A record of the $\delta^{44/40}Ca$ and [Sr] of seawater over the last 100 million years from fossil elasmobranch tooth enamel. *Earth Planet. Sci. Lett.* 543:116354

Aloisi G. 2015. Covariation of metabolic rates and cell size in coccolithophores. *Biogeosciences* 12:4665–92

Anagnostou E, John EH, Babila TL, Sexton PF, Ridgwell A, et al. 2020. Proxy evidence for state-dependence of climate sensitivity in the Eocene greenhouse. *Nat. Commun.* 11(1):1–9

Anagnostou E, John EH, Edgar KM, Foster GL, Ridgwell A, et al. 2016. Changing atmospheric CO_2 concentration was the primary driver of early Cenozoic climate. *Nature* 533(7603):380–84

Arrhenius S. 1896. On the influence of carbonic acid in the air upon the temperature of the ground. *Philos. Mag. J. Sci. Ser.* 5 41:237–76

Badger MPS, Chalk TB, Foster GL, Bown PR, Gibbs SJ, et al. 2019. Insensitivity of alkenone carbon isotopes to atmospheric CO_2 at low to moderate CO_2 levels. *Clim. Past* 15(2):539–54

Badger MPS, Lear CH, Pancost RD, Foster GL, Bailey TR, et al. 2013. CO_2 drawdown following the middle Miocene expansion of the Antarctic Ice Sheet. *Paleoceanography* 28(1):42–53

Beerling DJ, Royer DL. 2011. Convergent Cenozoic CO_2 history. *Nat. Geosci.* 4(7):418–20

Bereiter B, Eggleston S, Schmitt J, Nehrbass-Ahles C, Stocker TF, et al. 2015. Revision of the EPICA Dome C CO_2 record from 800 to 600 kyr before present. *Geophys. Res. Lett.* 42(2):542–49

Berner RA. 1991. A model for atmospheric CO_2 over Phanerozoic time. *Am. J. Sci.* 291(4):339–76

Berner RA, Caldeira K. 1997. The need for mass balance and feedback in the geochemical carbon cycle. *Geology* 25(10):955–53

Berner RA, Lasaga AC, Garrels RM. 1983. The carbonate-silicate geochemical cycle and its effect on atmospheric carbon dioxide over the past 100 million years. *Am. J. Sci.* 283:641–83

Bidigare RR, Fluegge A, Freeman KH, Hanson KL, Hayes JM, et al. 1997. Consistent fractionation of C-13 in nature and in the laboratory: growth-rate effects in some haptophyte algae. *Glob. Biogeochem. Cycles* 11(2):279–92

Blanco-Ameijeiras S, Stoll HM, Zhang H, Hopkinson BM. 2020. Influence of temperature and CO_2 on plasma-membrane permeability to CO_2 and HCO_3^- in the marine haptophytes *Emiliania huxleyi* and *Calcidiscus leptoporus* (Prymnesiophyceae). *J. Phycol.* 56:1283–94

Boller AJ, Thomas PJ, Cavanaugh CM, Scott KM. 2011. Low stable carbon isotope fractionation by coccolithophore RubisCO. *Geochim. Cosmochim. Acta* 75(22):7200–7

Bolton CT, Hernández-Sánchez MT. 2016. Decrease in coccolithophore calcification and CO_2 since the middle Miocene. *Nature* 7:10284

Bolton CT, Stoll HM. 2013. Late Miocene threshold response of marine algae to carbon dioxide limitation. *Nature* 500:558–62

Boudreau BP, Middelburg JJ, Meysman FJ. 2010. Carbonate compensation dynamics. *Geophys. Res. Lett.* 37(3):L03603

Boudreau BP, Middelburg JJ, Sluijs A, van der Ploeg R. 2019. Secular variations in the carbonate chemistry of the oceans over the Cenozoic. *Earth Planet. Sci. Lett.* 512:194–206

Branson O. 2018. Boron incorporation into marine $CaCO_3$. In *Boron Isotopes*, ed. H Marschall, G Foster, pp. 71–105. Cham, Switz.: Springer

Branson O, Bonnin EA, Perea DE, Spero HJ, Zhu Z, et al. 2016. Nanometer-scale chemistry of a calcite biomineralization template: implications for skeletal composition and nucleation. *PNAS* 113:12934–39

Brassell SC. 2014. Climatic influences on the Paleogene evolution of alkenones. *Paleoceanography* 29(3):255–72

Brennan ST, Lowenstein TK, Cendón DI. 2013. The major-ion composition of Cenozoic seawater: the past 36 million years from fluid inclusions in marine halite. *Am. J. Sci.* 313(8):713–75

Broecker WS. 2013. How to think about the evolution of the ratio of Mg to Ca in seawater. *Am. J. Sci.* 313(8):776–89

Broecker WS. 2015. *Wally's Carbon World*. Palisades, NY: Eldigio. **https://www.ldeo.columbia.edu/~broecker/Carbon%20World%20.pdf**

Broecker WS, Peng T-H. 1987. The role of $CaCO_3$ compensation in the glacial to interglacial atmospheric CO_2 change. *Glob. Biogeochem. Cycles* 1(1):15–29

Burke KD, Williams JW, Chandler MA, Haywood AM, Lunt DJ, Otto-Bliesner BL. 2018. Pliocene and Eocene provide best analogs for near-future climates. *PNAS* 115(52):13288–93

Caldeira K, Wickett ME. 2003. Anthropogenic carbon and ocean pH. *Nature* 425:365

Campbell SM, Moucha R, Derry LA, Raymo ME. 2018. Effects of dynamic topography on the Cenozoic carbonate compensation depth. *Geochem. Geophys. Geosyst.* 19(4):1025–34

Caves Rugenstein JK, Ibarra DE, von Blanckenburg F. 2019. Neogene cooling driven by land surface reactivity rather than increased weathering fluxes. *Nature* 571(7763):99–102

Chalk TB, Hain MP, Foster GL, Rohling EJ, Sexton PF, et al. 2017. Causes of ice age intensification across the Mid-Pleistocene Transition. *PNAS* 114(50):13114–19

Chen B, Liu H. 2010. Relationships between phytoplankton growth and cell size in surface oceans: interactive effects of temperature, nutrients, and grazing. *Limnol. Oceanogr.* 55(3):965–72

de la Vega E, Chalk TB, Wilson PA, Bysani RP, Foster GL. 2020. Atmospheric CO_2 during the mid-Piacenzian Warm Period and the M2 glaciation. *Sci. Rep.* 10:11002

Dean WE, Arthur MA, Claypool GE. 1986. Depletion of ^{13}C in Cretaceous marine organic matter: source, diagenetic, or environmental sigal? *Mar. Geol.* 70(1–2):119–57

Dickson AG. 1990. Thermodynamics of the dissociation of boric acid in synthetic seawater from 273.15 to 318.15 K. *Deep Sea Res. A Oceanogr. Res. Pap.* 37(5):755–66

Dutton A, Carlson AE, Long AJ, Milne GA, Clark PU, et al. 2015. Sea-level rise due to polar ice-sheet mass loss during past warm periods. *Science* 349(6244):aaa4019

Dyez KA, Hönisch B, Schmidt GA. 2018. Early Pleistocene obliquity-scale pCO_2 variability at ∼1.5 million years ago. *Paleoceanogr. Paleoclimatol.* 33(11):1270–91

Eberle JJ, Greenwood DR. 2012. Life at the top of the greenhouse Eocene world—a review of the Eocene flora and vertebrate fauna from Canada's High Arctic. *Bulletin* 124(1–2):3–23

Edmond JM, Huh Y. 1997. Chemical weathering yields from basement and orogenic terrains in hot and cold climates. In *Tectonic Uplift and Climate Change*, ed. WF Ruddiman, pp. 329–51. Boston: Springer

Evans D, Sagoo N, Renema W, Cotton LJ, Müller W, et al. 2018. Eocene greenhouse climate revealed by coupled clumped isotope-Mg/Ca thermometry. *PNAS* 115:1174–79

Farnsworth A, Lunt DJ, O'Brien CL, Foster GL, Inglis GN, et al. 2019. Climate sensitivity on geological timescales controlled by nonlinear feedbacks and ocean circulation. *Geophys. Res. Lett.* 46(16):9880–89

Finkel ZV, Beardall J, Flynn KJ, Quigg A, Rees TAV, Raven JA. 2010. Phytoplankton in a changing world: cell size and elemental stoichiometry. *J. Plankton Res.* 32(1):119–37

Foote E. 1856. Circumstances affecting the heat of the sun's rays. *Am. J. Sci. Arts* 22:382–83

Foster GL. 2008. Seawater pH, pCO_2 and $[CO^{2-}_3]$ variations in the Caribbean Sea over the last 130 kyr: a boron isotope and B/Ca study of planktic foraminifera. *Earth Planet. Sci. Lett.* 271(1–4):254–66

Foster GL, Hoenisch B, Paris G, Dwyer GS, Rae JWB, et al. 2013. Interlaboratory comparison of boron isotope analyses of boric acid, seawater and marine $CaCO_3$ by MC-ICPMS and NTIMS. *Chem. Geol.* 358:1–14

Foster GL, Lear CH, Rae JWB. 2012. The evolution of pCO2, ice volume and climate during the middle Miocene. *Earth Planet. Sci. Lett.* 341:243–54

Foster GL, Pogge von Strandmann PAE, Rae JWB. 2010. Boron and magnesium isotopic composition of seawater. *Geochem. Geophys. Geosyst.* 11(8):Q08015

Foster GL, Rae JWB. 2016. Reconstructing ocean pH with boron isotopes in foraminifera. *Annu. Rev. Earth Planet. Sci.* 44:207–37

Freeman KH, Hayes JM. 1992. Fractionation of carbon isotopes by phytoplankton and estimates of ancient CO_2 levels. *Glob. Biogeochem. Cycles* 6(2):185–98

Gattuso J-P, Epitalon J-M, Lavigne H, Orr J, Gentili B, et al. 2015a. seacarb: seawater carbonate chemistry. *R. Package Version* 3(1), **https://hal.u-pec.fr/UMS-829/hal-02345814v1**

Gattuso J-P, Magnan A, Billé R, Cheung WW, Howes EL, et al. 2015b. Contrasting futures for ocean and society from different anthropogenic CO_2 emissions scenarios. *Science* 349(6243):aac4722

Gray WR, Evans D. 2019. Nonthermal influences on Mg/Ca in planktonic foraminifera: a review of culture studies and application to the Last Glacial Maximum. *Paleoceanogr. Paleoclimatol.* 34(3):306–15

Greene SE, Ridgwell A, Kirtland Turner S, Schmidt DN, Pälike H, et al. 2019. Early Cenozoic decoupling of climate and carbonate compensation depth trends. *Paleoceanogr. Paleoclimatol.* 34(6):930–45

Greenop R, Foster GL, Wilson PA, Lear CH. 2014. Middle Miocene climate instability associated with high-amplitude CO_2 variability. *Paleoceanography* 29(9):845–53

Greenop R, Hain MP, Sosdian S, Oliver KIC, Goodwin P, et al. 2017. A record of Neogene seawater $\delta^{11}B$ reconstructed from paired $\delta^{11}B$ analyses on benthic and planktic foraminifera. *Clim. Past* 13:149–70

Greenop R, Sosdian SM, Henehan MJ, Wilson PA, Lear CH, Foster GL. 2019. Orbital forcing, ice volume, and CO_2 across the Oligocene-Miocene transition. *Paleoceanogr. Paleoclimatol.* 34(3):316–28

Gutjahr M, Bordier L, Douville E, Farmer J, Foster GL, et al. 2020. Sub-permil interlaboratory consistency for solution-based boron isotope analyses on marine carbonates. *Geostand. Geoanal. Res.* 41:90–17

Gutjahr M, Ridgwell A, Sexton PF, Anagnostou E, Pearson PN, et al. 2017. Very large release of mostly volcanic carbon during the Palaeocene–Eocene Thermal Maximum. *Nature* 548(7669):573–77

Hain MP, Foster GL, Chalk T. 2018. Robust constraints on past CO_2 climate forcing from the boron isotope proxy. *Paleoceanogr. Paleoclimatol.* 33(10):1099–115

Hain MP, Sigman DM, Higgins JA, Haug GH. 2015. The effects of secular calcium and magnesium concentration changes on the thermodynamics of seawater acid/base chemistry: implications for Eocene and Cretaceous ocean carbon chemistry and buffering. *Glob. Biogeochem. Cycles* 29(5):517–33

Hansen J, Sato M, Russell G, Kharecha P. 2013. Climate sensitivity, sea level and atmospheric carbon dioxide. *Philos. Trans. R. Soc. A* 371(2001):20120294

Harper DT, Hönisch B, Zeebe RE, Shaffer G, Haynes LL, et al. 2020. The magnitude of surface ocean acidification and carbon release during Eocene Thermal Maximum 2 (ETM-2) and the Paleocene-Eocene Thermal Maximum (PETM). *Paleoceanogr. Paleoclimatol.* 35(2):e2019PA003699

Hausfather Z, Peters GP. 2020. Emissions—the "business as usual" story is misleading. *Nature* 577:618–20

Hayes JM, Freeman KH, Popp BN, Hoham CH. 1990. Compound-specific isotopic analyses: a novel tool for reconstruction of ancient biogeochemical processes. *Org. Geochem.* 16(4–6):1115–28

Hemming NG, Hanson GN. 1992. Boron isotopic composition and concentration in modern marine carbonates. *Geochim. Cosmochim. Acta* 56:537–43

Henderiks J, Pagani M. 2007. Refining ancient carbon dioxide estimates: significance of coccolithophore cell size for alkenone-based pCO$_2$ records. *Paleoceanography* 22(3):PA3202

Henehan MJ, Edgar KM, Foster GL, Penman DE, Hull PM, et al. 2020. Revisiting the Middle Eocene Climatic Optimum "carbon cycle conundrum" with new estimates of atmospheric pCO$_2$ from boron isotopes. *Paleoceanogr. Paleoclimatol.* 35(6):2019PA003713

Henehan MJ, Foster GL, Bostock HC, Greenop R, Marshall BJ, Wilson PA. 2016a. A new boron isotope-pH calibration for *Orbulina universa*, with implications for understanding and accounting for "vital effects." *Earth Planet. Sci. Lett.* 454:282–92

Henehan MJ, Hull PM, Penman DE, Rae JWB, Schmidt DN. 2016b. Biogeochemical significance of pelagic ecosystem function: an end-Cretaceous case study. *Philos. Trans. R. Soc. B* 371(1694):20150510

Henehan MJ, Rae JWB, Foster GL, Erez J, Prentice KC, et al. 2013. Calibration of the boron isotope proxy in the planktonic foraminifera *Globigerinoides ruber* for use in palaeo-CO$_2$ reconstruction. *Earth Planet. Sci. Lett.* 364:111–22

Henehan MJ, Ridgwell A, Thomas E, Zhang S, Alegret L, et al. 2019. Rapid ocean acidification and protracted Earth system recovery followed the end-Cretaceous Chicxulub impact. *PNAS* 116(45):22500–4

Herbert TD, Lawrence KT, Tzanova A, Peterson LC, Caballero-Gill R, Kelly CS. 2016. Late Miocene global cooling and the rise of modern ecosystems. *Nat. Geosci.* 9(11):843–47

Hernandez-Almeida I, Krumhardt KM, Zhang H, Stoll HM. 2020. Estimation of physiological factors controlling carbon isotope fractionation in coccolithophores in photic zone and core-top samples. *Geochem. Geophys. Geosyst.* 21(11):e2020GC009272

Heureux AMC, Rickaby REM. 2015. Refining our estimate of atmospheric CO_2 across the Eocene–Oligocene climatic transition. *Earth Planet. Sci. Lett.* 409:329–38

Holtz L-M, Wolf-Gladrow D, Thoms S. 2017. Stable carbon isotope signals in particulate organic and inorganic carbon of coccolithophores—a numerical model study for *Emiliania huxleyi*. *J. Theor. Biol.* 420:117–27

Hönisch B, Eggins SM, Haynes LL, Allen KA, Holland KD, Lorbacher K. 2019. *Boron Proxies in Paleoceanography and Paleoclimatology*. Hoboken, NJ: Wiley & Sons

Hönisch B, Hemming NG. 2005. Surface ocean pH response to variations in pCO$_2$ through two full glacial cycles. *Earth Planet. Sci. Lett.* 236(1–2):305–14

Hönisch B, Hemming NG, Archer D, Siddall M, McManus JF. 2009. Atmospheric carbon dioxide concentration across the mid-Pleistocene transition. *Science* 324(5934):1551–54

Hönisch B, Ridgwell A, Schmidt DN, Thomas E, Gibbs SJ, et al. 2012. The geological record of ocean acidification. *Science* 335(6072):1058–63

Hopkinson BM, Dupont CL, Allen AE, Morel FM. 2011. Efficiency of the CO_2-concentrating mechanism of diatoms. *PNAS* 108(10):3830–37

Horita J, Zimmermann H, Holland HD. 2002. Chemical evolution of seawater during the Phanerozoic: implications from the record of marine evaporites. *Geochim. Cosmochim. Acta* 66(21):3733–56

Inglis GN, Bragg F, Burls N, Evans D, Foster GL, et al. 2020. Global mean surface temperature and climate sensitivity of the EECO, PETM and latest Paleocene. *Clim. Past* 16:1953–68

Inglis GN, Farnsworth A, Lunt D, Foster GL, Hollis CJ, et al. 2015. Descent toward the Icehouse: Eocene sea surface cooling inferred from GDGT distributions. *Paleoceanography* 30:1000–20

Isson TT, Planavsky NJ, Coogan LA, Stewart EM, Ague JJ, et al. 2020. Evolution of the global carbon cycle and climate regulation on Earth. *Glob. Biogeochem. Cycles* 34(2):e2018GB006061

Jasper JP, Hayes JM. 1990. A carbon isotope record of CO_2 levels during the late Quaternary. *Nature* 347(6292):462–64

Jurikova H, Gutjahr M, Wallmann K, Flogel S, Liebetrau V, et al. 2020. Permian–Triassic mass extinction pulses driven by major marine carbon cycle perturbations. *Nat. Geosci.* 13(11):745–50

Jurikova H, Liebetrau V, Gutjahr M, Rollion-Bard C, Hu MY, et al. 2019. Boron isotope systematics of cultured brachiopods: response to acidification, vital effects and implications for palaeo-pH reconstruction. *Geochim. Cosmochim. Acta* 248:370–86

Kasting JF. 2019. The Goldilocks planet? How silicate weathering maintains Earth "just right." *Elements* 15(4):235–40

Klochko K, Kaufman AJ, Yao W, Byrne RH, Tossell JA. 2006. Experimental measurement of boron isotope fractionation in seawater. *Earth Planet. Sci. Lett.* 248(1–2):276–85

Kump LR, Brantley SL, Arthur M. 2000. Chemical weathering, atmospheric CO_2, and climate. *Annu. Rev. Earth Planet. Sci.* 28:611–67

Kürschner WM, Kvaček Z, Dilcher DL. 2008. The impact of Miocene atmospheric carbon dioxide fluctuations on climate and the evolution of terrestrial ecosystems. *PNAS* 105(2):449–53

Lacis AA, Schmidt GA, Rind D, Ruedy RA. 2010. Atmospheric CO_2: principal control knob governing Earth's temperature. *Science* 330(6002):356–59

Laws EA, Popp BN, Bidigare RR, Kennicutt MC, Macko SA. 1995. Dependence of phytoplankton carbon isotopic composition on growth rate and $[CO_2]_{aq}$: theoretical considerations and experimental results. *Geochim. Cosmochim. Acta* 59(6):1131–38

Lear CH, Elderfield H, Wilson PA. 2000. Cenozoic deep-sea temperatures and global ice volumes from Mg/Ca in benthic foraminiferal calcite. *Science* 287(5451):269–72

Lemarchand D, Gaillardet J, Lewin É, Allègre CJ. 2000. The influence of rivers on marine boron isotopes and implications for reconstructing past ocean pH. *Nature* 408(6815):951–54

Li G, Hartmann J, Derry LA, West AJ, You C-F, et al. 2016. Temperature dependence of basalt weathering. *Earth Planet. Sci. Lett.* 443:59–69

Lowenstein TK, Hardie LA, Timofeef MN, Demicco RV. 2003. Secular variation in seawater chemistry and the origin of calcium chloride basinal brines. *Geology* 31:857–60

Lunt DJ, Farnsworth A, Loptson C, Foster GL, Markwick P, et al. 2016. Palaeogeographic controls on climate and proxy interpretation. *Clim. Past* 12(5):1181–98

Martínez-Botí MA, Foster GL, Chalk TB, Rohling EJ, Sexton PF, et al. 2015. Plio-Pleistocene climate sensitivity evaluated using high-resolution CO_2 records. *Nature* 518(7537):49–54

Mason E, Edmonds M, Turchyn AV. 2017. Remobilization of crustal carbon may dominate volcanic arc emissions. *Science* 357(6348):290–94

Masson-Delmotte V, Zhai P, Pörtner H-O, Roberts D, Skea J, et al. 2018. *Global warming of 1.5°C: An IPCC Special Report on the impacts of global warming of 1.5°C above pre-industrial levels and related global greenhouse gas emission pathways, in the context of strengthening the global response to the threat of climate change, sustainable development, and efforts to eradicate poverty*. Rep. World Meteorol. Organ., Geneva

McClelland H, Bruggeman J, Hermoso M, Rickaby R. 2017. The origin of carbon isotope vital effects in coccolith calcite. *Nat. Commun.* 8(1):1–16

McClymont EL, Ford HL, Ho SL, Tindall JC, Haywood AM, et al. 2020. Lessons from a high-CO_2 world: an ocean view from ~3 million years ago. *Clim. Past* 16(4):1599–615

McCulloch M, Trotter J, Montagna P, Falter J, Dunbar R, et al. 2012. Resilience of cold-water scleractinian corals to ocean acidification: boron isotopic systematics of pH and saturation state up-regulation. *Geochim. Cosmochim. Acta* 87:21–34

Meinshausen M, Nicholls Z, Lewis J, Gidden MJ, Vogel E, et al. 2019. The SSP greenhouse gas concentrations and their extensions to 2500. *Geosci. Model. Dev. Discuss.* 2019:1–77

Mejía LM, Mendez-Vicente A, Abrevaya L, Lawrence KT, Ladlow C, et al. 2017. A diatom record of CO_2 decline since the late Miocene. *Earth Planet. Sci. Lett.* 479:18–33

Middelburg JJ, Soetaert K, Hagens M. 2020. Ocean alkalinity, buffering and biogeochemical processes. *Rev. Geophys.* 58(3):e2019RG000681

Miller KG, Browning JV, Schmelz WJ, Kopp RE, Mountain GS, Wright JD. 2020. Cenozoic sea-level and cryospheric evolution from deep-sea geochemical and continental margin records. *Sci. Adv.* 6(20):eaaz1346

Misra S, Froelich PN. 2012. Lithium isotope history of Cenozoic seawater: changes in silicate weathering and reverse weathering. *Science* 335(6070):818–23

Müller T, Jurikova H, Gutjahr M, Tomašových A, Schlögl J, et al. 2020. Ocean acidification during the early Toarcian extinction event: evidence from boron isotopes in brachiopods. *Geology* 48(12)1184–88

Naafs B, Castro JM, De Gea GA, Quijano ML, Schmidt DN, Pancost RD. 2016. Gradual and sustained carbon dioxide release during Aptian Oceanic Anoxic Event 1a. *Nat. Geosci.* 9(2):135–39

Nir O, Vengosh A, Harkness JS, Dwyer GS, Lahav O. 2015. Direct measurement of the boron isotope fractionation factor: reducing the uncertainty in reconstructing ocean paleo-pH. *Earth Planet. Sci. Lett.* 414:1–5

Pagani M. 2002. The alkenone-CO_2 proxy and ancient atmospheric carbon dioxide. *Philos. Trans. R. Soc. A* 360:609–32

Pagani M, Freeman KH, Arthur MA. 1999. Late Miocene atmospheric CO_2 concentrations and the expansion of C_4 grasses. *Science* 285:876–79

Pagani M, Huber M, Liu Z, Bohaty SM, Henderiks J, et al. 2011. The role of carbon dioxide during the onset of Antarctic glaciation. *Science* 334(6060):1261–64

Pagani M, Liu Z, LaRiviere J, Ravelo AC. 2010. High Earth-system climate sensitivity determined from Pliocene carbon dioxide concentrations. *Nat. Geosci.* 3(1):27–30

Pagani M, Zachos JC, Freeman KH, Tipple B, Bohaty S. 2005. Marked decline in atmospheric carbon dioxide concentrations during the Paleogene. *Science* 309(5734):600–3

Palike H, Lyle MW, Nishi H, Raffi I, Ridgwell A, et al. 2012. A Cenozoic record of the equatorial Pacific carbonate compensation depth. *Nature* 488(7413):609–14

Palmer MR, Pearson PN, Cobb SJ. 1998. Reconstructing past ocean pH-depth profiles. *Science* 282(5393):1468–71

Pancost RD, Freeman KH, Wakeham SG, Robertson CY. 1997. Controls on carbon isotope fractionation by diatoms in the Peru upwelling region. *Geochim. Cosmochim. Acta* 61(23):4983–91

Paris G, Gaillardet J, Louvat P. 2010. Geological evolution of seawater boron isotopic composition recorded in evaporites. *Geology* 38(11):1035–38

Pearson PN, Foster GL, Wade BS. 2009. Atmospheric carbon dioxide through the Eocene–Oligocene climate transition. *Nature* 461(7267):1110–13

Pearson PN, Palmer MR. 1999. Middle Eocene seawater pH and atmospheric carbon dioxide concentrations. *Science* 284:1824–26

Pearson PN, Palmer MR. 2000. Atmospheric carbon dioxide concentrations over the past 60 million years. *Nature* 406:695–99

Penman DE, Caves Rugenstein JK, Ibarra DE, Winnick MJ. 2020. Silicate weathering as a feedback and forcing in Earth's climate and carbon cycle. *Earth-Sci. Rev.* 209:103298

Penman DE, Hönisch B, Zeebe RE, Thomas E, Zachos JC. 2014. Rapid and sustained surface ocean acidification during the Paleocene-Eocene Thermal Maximum. *Paleoceanography* 29(5):357–69

Pogge von Strandmann PAE, Forshaw J, Schmidt DN. 2014. Modern and Cenozoic records of seawater magnesium from foraminiferal Mg isotopes. *Biogeosciences* 11(18):5155–68

Popp BN, Takigiku R, Hayes JM, Louda JW, Baker EW. 1989. The post-Paleozoic chronology and mechanism of ^{13}C depletion in primary marine organic matter. *Am. J. Sci.* 289(4):436–54

Popp BN, Laws EA, Bidigare RR, Dore JE, Hanson KL, Wakeham SG. 1998. Effect of phytoplankton cell geometry on carbon isotopic fractionation. *Geochim. Cosmochim. Acta* 62(1):69–77

Rae JWB. 2018. Boron isotopes in foraminifera: systematics, biomineralisation, and CO_2 reconstruction. In *Boron Isotopes*, ed. H Marschall, G Foster, pp. 107–43. Cham, Switz.: Springer

Rae JWB, Foster GL, Schmidt DN, Elliott T. 2011. Boron isotopes and B/Ca in benthic foraminifera: proxies for the deep ocean carbonate system. *Earth Planet. Sci. Lett.* 302(3):403–13

Raitzsch M, Bijma J, Benthien A, Richter K-U, Steinhoefel G, Kucera M. 2018. Boron isotope-based seasonal paleo-pH reconstruction for the Southeast Atlantic—a multispecies approach using habitat preference of planktonic foraminifera. *Earth Planet. Sci. Lett.* 487:138–50

Raitzsch M, Hönisch B. 2013. Cenozoic boron isotope variations in benthic foraminifers. *Geology* 41(5):591–94

Rau GH, Riebesell U, Wolf-Gladrow D. 1996. A model of photosynthetic ^{13}C fractionation by marine phytoplankton based on diffusive molecular CO_2 uptake. *Mar. Ecol. Prog. Ser.* 133:275–85

Raymo ME, Kozdon R, Evans D, Lisiecki L, Ford HL. 2018. The accuracy of mid-Pliocene δ^{18}O-based ice volume and sea level reconstructions. *Earth-Sci. Rev.* 177:291–302

Raymo ME, Ruddiman WF. 1992. Tectonic forcing of late Cenozoic climate. *Nature* 359:117–22

Rees-Owen RL, Gill FL, Newton RJ, Ivanovic RF, Francis JE, et al. 2018. The last forests on Antarctica: reconstructing flora and temperature from the Neogene Sirius Group, Transantarctic Mountains. *Org. Geochem.* 118:4–14

Ridgwell A. 2005. A Mid Mesozoic Revolution in the regulation of ocean chemistry. *Mar. Geol.* 217(3–4):339–57

Rohling EJ, Sluijs A, Dijkstra HA, Köhler P, van de Wal R, et al. 2012. Making sense of palaeoclimate sensitivity. *Nature* 491:683–91

Royer DL. 2016. Climate sensitivity in the geologic past. *Annu. Rev. Earth Planet. Sci.* 44:277–93

Sanyal A, Bijma J, Spero HJ, Lea D. 2001. Empirical relationship between pH and the boron isotopic composition of *Globigerinoides sacculifer*: implications for the boron isotope paleo-pH proxy. *Paleoceanography* 16(5):515–19

Sanyal A, Hemming NG, Broecker WS, Lea DW, Spero HJ, Hanson GN. 1996. Oceanic *p*H control on the boron isotopic composition of foraminifera: evidence from culture experiments. *Paleoceanography* 11(5):513–17

Sarmiento JL, Gruber N. 2006. *Ocean Biogeochemical Dynamics*. Princeton, NJ: Princeton Univ. Press

Schneider T, Kaul CM, Pressel KG. 2019. Possible climate transitions from breakup of stratocumulus decks under greenhouse warming. *Nat. Geosci.* 12(3):163–67

Seki O, Foster GL, Schmidt DN, Mackensen A, Kawamura K, Pancost RD. 2010. Alkenone and boron-based Pliocene *p*CO$_2$ records. *Earth Planet. Sci. Lett.* 292(1–2):201–11

Sherman E, Moore JK, Primeau F, Tanouye D. 2016. Temperature influence on phytoplankton community growth rates. *Glob. Biogeochem. Cycles* 30(4):550–59

Sherwood S, Webb MJ, Annan JD, Armour KC, Forster PM, et al. 2020. An assessment of Earth's climate sensitivity using multiple lines of evidence. *Rev. Geophys.* 58(4):e2019RG000678

Sluijs A, van Roij L, Frieling J, Laks J, Reichart G-J. 2018. Single-species dinoflagellate cyst carbon isotope ecology across the Paleocene-Eocene Thermal Maximum. *Geology* 46(1):79–82

Sosdian SM, Greenop R, Hain MP, Foster GL, Pearson PN, Lear CH. 2018. Constraining the evolution of Neogene ocean carbonate chemistry using the boron isotope pH proxy. *Earth Planet. Sci. Lett.* 498:362–76

Stewart JA, Christopher SJ, Kucklick JR, Bordier L, Chalk TB, et al. 2020. NIST RM 8301 boron isotopes in marine carbonate (simulated coral and foraminifera solutions): inter-laboratory δ^{11}B and trace element ratio value assignment. *Geostand. Geoanal. Res.* 513(05):143–20

Stoll HM, Guitian J, Hernandez-Almeida I, Mejía LM, Phelps S, et al. 2019. Upregulation of phytoplankton carbon concentrating mechanisms during low CO_2 glacial periods and implications for the phytoplankton pCO$_2$ proxy. *Quat. Sci. Rev.* 208:1–20

Super JR, Thomas E, Pagani M, Huber M, O'Brien CL, Hull PM. 2018. North Atlantic temperature and pCO2 coupling in the early-middle Miocene. *Geology* 46(6):519–22

Takahashi T, Sutherland SC, Chipman DW, Goddard JG, Ho C, et al. 2014. Climatological distributions of pH, pCO_2, total CO_2, alkalinity, and $CaCO_3$ saturation in the global surface ocean, and temporal changes at selected locations. *Mar. Chem.* 164:95–125

Tierney JE, Haywood AM, Feng R, Bhattacharya T, Otto-Bliesner BL. 2019a. Pliocene warmth consistent with greenhouse gas forcing. *Geophys. Res. Lett.* 46(15):9136–44

Tierney JE, Malevich SB, Gray W, Vetter L, Thirumalai K. 2019b. Bayesian calibration of the Mg/Ca paleothermometer in planktic foraminifera. *Paleoceanogr. Paleoclimatol.* 34(12):2005–30

Tierney JE, Poulsen CJ, Montanez IP, Bhattacharya T, Feng R, et al. 2020a. Past climates inform our future. *Science* 370(6517):eaay3701

Tierney JE, Zhu J, King J, Malevich SB, Hakim GJ, Poulsen CJ. 2020b. Glacial cooling and climate sensitivity revisited. *Nature* 584:569–73

Timofeeff MN, Lowenstein TK, da Silva MAM, Harris NB. 2006. Secular variation in the major-ion chemistry of seawater: evidence from fluid inclusions in Cretaceous halites. *Geochim. Cosmochim. Acta* 70(8):1977–94

Torres MA, Moosdorf N, Hartmann J, Adkins JF, West AJ. 2017. Glacial weathering, sulfide oxidation, and global carbon cycle feedbacks. *PNAS* 114(33):8716–21

Tyrrell T, Zeebe RE. 2004. History of carbonate ion concentration over the last 100 million years. *Geochim. Cosmochim. Acta* 68(17):3521–30

Urey HC. 1952. On the early chemical history of the earth and the origin of life. *PNAS* 38(4):351–63

van Heuven S, Pierrot D, Rae JWB, Lewis E, Wallace DWR. 2009. MATLAB program developed for CO2 system calculations, Vol. ORNL/CDIAC-105b. *Carbon Dioxide Information Analysis Center*, *Oak Ridge National Laboratory, U.S. Department of Energy*. **https://cdiac.ess-dive.lbl.gov/ftp/co2sys/CO2SYS_calc_MATLAB_v1.1/**

Westerhold T, Marwan N, Drury AJ, Liebrand D, Agnini C, et al. 2020. An astronomically dated record of Earth's climate and its predictability over the last 66 million years. *Science* 369(6509):1383–87

Wilkes EB, Lee RB, McClelland HL, Rickaby RE, Pearson A. 2018. Carbon isotope ratios of coccolith–associated polysaccharides of *Emiliania huxleyi* as a function of growth rate and CO_2 concentration. *Org. Geochem.* 119:1–10

Wilkes EB, Pearson A. 2019. A general model for carbon isotopes in red-lineage phytoplankton: interplay between unidirectional processes and fractionation by RubisCO. *Geochim. Cosmochim. Acta* 265:163–81

Witkowski CR, Weijers JW, Blais B, Schouten S, Damsté JS. 2018. Molecular fossils from phytoplankton reveal secular P_{CO_2} trend over the Phanerozoic. *Sci. Adv.* 4(11):eaat4556

Zachos JC, Dickens GR, Zeebe RE. 2008. An early Cenozoic perspective on greenhouse warming and carbon-cycle dynamics. *Nature* 451(7176):279–83

Zachos JC, Pagani M, Sloan L, Thomas E, Billups K. 2001. Trends, rhythms, and aberrations in global climate 65 Ma to present. *Science* 292:686–93

Zeebe RE. 2012. History of seawater carbonate chemistry, atmospheric CO_2, and ocean acidification. *Annu. Rev. Earth Planet. Sci.* 40:141–65

Zeebe RE, Ridgwell A, Zachos JC. 2016. Anthropogenic carbon release rate unprecedented during the past 66 million years. *Nat. Geosci.* 9(4):325–29

Zeebe RE, Tyrrell T. 2019. History of carbonate ion concentration over the last 100 million years II: revised calculations and new data. *Geochim. Cosmochim. Acta* 257:373–92

Zeebe RE, Wolf-Gladrow DA. 2001. *CO_2 in Seawater: Equilibrium, Kinetics, Isotopes*. Amsterdam: Elsevier

Zhang YG, Henderiks J, Liu X. 2020. Refining the alkenone-pCO_2 method II: towards resolving the physiological parameter '*b*.' *Geochim. Cosmochim. Acta* 281:118–34

Zhang YG, Pagani M, Henderiks J, Ren H. 2017. A long history of equatorial deep-water upwelling in the Pacific Ocean. *Earth Planet. Sci. Lett.* 467:1–9

Zhang YG, Pagani M, Liu Z, Bohaty SM, DeConto R. 2013. A 40-million-year history of atmospheric CO_2. *Philos. Trans. R. Soc. A* 371(2001):20130096

Zhang YG, Pearson A, Benthien A, Dong L, Huybers P, et al. 2019. Refining the alkenone-pCO2 method I: lessons from the Quaternary glacial cycles. *Geochim. Cosmochim. Acta* 260:177–91

Zhu J, Poulsen CJ, Tierney JE. 2019. Simulation of Eocene extreme warmth and high climate sensitivity through cloud feedbacks. *Sci. Adv.* 5(9):eaax1874

RELATED RESOURCES

Palaeo-CO$_2$ Project: **http://www.p-co2.org/**. Web resources on CO$_2$ reconstruction from marine archives, containing the data collated here and future updates and iterations

Paleo-CO$_2$: **https://www.paleo-co2.org/**. Web resources on CO$_2$ reconstruction from a wide variety of different archives

Scripps CO$_2$ Program: **https://scrippsco2.ucsd.edu/**. Modern CO$_2$ data

Contents

Errata

An online log of corrections to *Annual Review of Earth and Planetary Sciences* articles
may be found at http://www.annualreviews.org/errata/earth